

ON THE STELLAR POPULATIONS IN FAINT RED GALAXIES IN THE *HUBBLE* ULTRA DEEP FIELD

AMELIA M. STUTZ, CASEY PAPOVICH², DANIEL J. EISENSTEIN

Department of Astronomy and Steward Observatory, University of Arizona, 933 North Cherry Avenue, Tucson, Arizona 85721
 astutz, papovich, eisenstein@as.arizona.edu

Draft version November 7, 2021

ABSTRACT

We study the nature of faint, red-selected galaxies at $z \sim 2 - 3$ using the *Hubble* Ultra Deep Field (UDF) and *Spitzer* Infrared Array Camera (IRAC) photometry. Given the magnitude limit of the *HST* data, we detect candidate galaxies to $H_{AB} < 26$ mag, probing lower-luminosity (lower mass) galaxies at these redshifts. We identify 32 galaxies satisfying the $(J_{110} - H_{160})_{AB} > 1.0$ mag color selection, 16 of which have unblended $[3.6\mu\text{m}]$ and $[4.5\mu\text{m}]$ photometry from *Spitzer*. Using this multiwavelength dataset we derive photometric redshifts, masses, and stellar population parameters for these objects. We find that the selected objects span a diverse range of properties over a large range of redshifts, $1 \lesssim z \lesssim 3.5$. A substantial fraction (11/32) of the $(J_{110} - H_{160})_{AB} > 1$ mag population appear to be lower-redshift ($z \lesssim 2.5$), heavily obscured dusty galaxies or edge-on spiral galaxies, while others (12/32) appear to be galaxies at $2 \lesssim z \lesssim 3.5$ whose light at rest-frame optical wavelengths is dominated by evolved stellar populations. We argue that longer wavelength data ($\gtrsim 1 \mu\text{m}$, rest-frame) are essential for interpreting the properties of the stellar populations in red-selected galaxies at these redshifts. Interestingly, by including *Spitzer* data many candidates for galaxies dominated by evolved stellar populations are rejected, and for only a subset of the sample (6/16) do the data favor this interpretation. These objects have a surface density of $\sim 1 \text{ arcmin}^{-2}$. We place an upper limit on the space density of candidate massive evolved galaxies with $2.5 < z < 3.5$ and $H_{160}(AB) \leq 26$ mag of $n = 6.6^{+2.0}_{-3.0} \times 10^{-4} \text{ Mpc}^{-3}$ with a corresponding upper limit on the stellar mass density of $\rho^* = 5.6^{+4.4}_{-2.8} \times 10^7 M_{\odot} \text{ Mpc}^{-3}$. The $z > 2.5$ objects that are dominated by evolved stellar populations have a space density at most one-third that of $z \sim 0$ red, early-type galaxies. Therefore, at least two-thirds of present-day early-type galaxies assemble or evolve into their current configuration at redshifts below 2.5. We find a dearth of candidates for low-mass ($\lesssim 2 \times 10^{10} M_{\odot}$) galaxies at $1.5 < z \lesssim 3$ that are dominated by passively evolving stellar populations even though the data should be sensitive to them; thus, at these redshifts, galaxies whose light is dominated by evolved stellar populations are restricted to only those galaxies that have assembled high stellar mass.

Subject headings: cosmology: observations – galaxies: evolution – galaxies: high-redshift – galaxies: stellar content – infrared: galaxies

1. INTRODUCTION

In the hierarchical picture of galaxy evolution, galaxies assemble within dark matter haloes that merge over time (e.g., Freedman et al. 2001; Spergel et al. 2003). This model has been highly successful at reproducing galaxy clustering properties based on well-understood gravitational physics (e.g., Weinberg et al. 2004). However, it is difficult to test how galaxies assemble their stellar content within the context of these models because of uncertain physics coupling the dark matter and baryonic matter in these haloes.

Observationally, the cosmic star-formation-rate (SFR) density rises by roughly an order of magnitude from $z \sim 0$ to 1 and remains roughly constant from $z \sim 1$ –6 (Hopkins 2004, and references therein). At the same time, roughly half of the stellar-mass density in galaxies formed between $z \sim 3$ and 1, corresponding to this

peak in the SFR density (e.g., Dickinson et al. 2003; Rudnick et al. 2003; Glazebrook et al. 2004). While theoretical models broadly reproduce this evolution in the global galaxy population (e.g., Somerville et al. 2001; Hernquist & Springel 2003), they have difficulty in reproducing star-formation trends in individual galaxies, particularly in accounting for the formation and evolution of specific SFRs of the most massive objects (Baugh et al. 2003; Somerville et al. 2004; De Lucia et al. 2006; Croton et al. 2006). In particular, it is difficult for models to produce galaxies (at any redshift) that are mostly devoid of current star-formation and evolve only passively (e.g., Croton et al. 2006; Davé 2005). Quantifying the number of passively evolving galaxies — and as a function of redshift and stellar mass — is helpful for constraining the processes that form stars within galaxies.

Searches for high-redshift galaxies that are dominated by older, passively evolving stellar populations are challenging. The light from these stars peaks at rest-frame optical and near-IR wavelengths ($\simeq 0.4 - 2 \mu\text{m}$), which at $z \gtrsim 1$ are shifted into the observed-frame near-IR. Several surveys have used deep, near-IR observations to search for galaxies up to $z \sim 1 - 2$ whose light is dominated by older stellar populations (see e.g., McCarthy

¹ This work is based in part on observations taken with the NASA/ESA Hubble Space Telescope, which is operated by the Association of Universities for Research in Astronomy, Inc. (AURA) under NASA contract NAS5-26555; and on observations made with the *Spitzer Space Telescope*, which is operated by the Jet Propulsion Laboratory, California Institute of Technology, under NASA contract 1407.

² *Spitzer* Fellow

2004). Such objects should have very red $R - K$ colors, which span the 4000Å/Balmer-break at these redshifts; several searches have focused on so-called extremely red objects (EROs), with selected objects typically satisfying $(R - K)_{\text{Vega}} \gtrsim 5$ mag. As a class, EROs include both passively evolving early-type galaxies up to $z \sim 1$ (e.g., Cimatti et al. 2002) and dust-reddened starbursts (e.g., Smail et al. 2002). However, with only optical and near-IR photometry, it was not possible to uniquely interpret the majority of these objects (e.g., Moustakas et al. 2004; Wilson et al. 2007). Recent observations at longer wavelengths from *Spitzer* indicate that more than half of the ERO population have strong emission in the thermal IR (Wilson et al. 2004; Yan et al. 2004b), suggesting that such objects constitute a significant portion of the red-selected galaxy population.

Recently, observers have used deep near-IR data to study red-selected galaxies at higher redshifts. Franx et al. (2003) used deep VLT/ISAAC JHK_s observations to identify a population of “distant red galaxies” (DRGs) with $(J_s - K_s)_{\text{Vega}} > 2.3$ mag, which should select galaxies that have a strong Balmer/4000 Å break between the J_s and K_s bands at $z \sim 2-3.5$ (see also Saracco et al. 2001). Like EROs, the DRG color selection is also sensitive to high redshift ($z \gtrsim 1$) galaxies dominated by dust-enshrouded starbursts also have red observed $J - K$ colors (e.g., Smail et al. 2002). Indeed, subsequent study of DRGs has shown that the majority are massive galaxies that are actively forming stars at $z \sim 1.5-3$ (van Dokkum et al. 2003; Förster Schreiber et al. 2004; Rubin et al. 2004; Knudsen et al. 2005; Reddy et al. 2005; Papovich et al. 2006; Webb et al. 2006), and only a small subset appear to be completely devoid of star formation and passively evolving (Labbé et al. 2005; Kriek et al. 2006).

However, nearly all surveys of red-selected objects have been restricted to using near-IR images from ground-based telescopes, which in practice limits these searches to $K_{\text{AB}} \lesssim 24$ mag (e.g., Labbé et al. 2003). For passively evolving stellar populations at $z \sim 3$, this magnitude limit acts as a limit in *stellar mass* of $\gtrsim 10^{11} M_{\odot}$. In contrast, the $z \sim 2-3.5$ UV-selected, star-forming galaxies (so-called Lyman-break galaxies, LBGs) that dominate the SFR density (Reddy et al. 2005) have typical stellar masses $\sim 10^{10} M_{\odot}$ (for “ L^* ” LBGs; Papovich et al. 2001). The inferred ages for LBGs are generally less than 1 Gyr (Shapley et al. 2001, 2005) — significantly less than the age of the Universe at these epochs. Thus, it is unknown if there exists a population of “faded” LBGs, identifiable as red, passively evolving galaxies with stellar masses $\sim 10^{10} M_{\odot}$. Deriving constraints on the density of such objects would improve our understanding of the evolution of these galaxies and on how galaxies assemble their stellar content at these early epochs. However, detecting lower-mass, red galaxies at high redshift requires near-IR surveys with higher sensitivity than what is practically available from the ground.

Here, we use observations in the *Hubble* Ultra Deep Field (HUDF; Beckwith et al. 2006 and Thompson et al. 2005). This field has the deepest optical *HST*/ACS images to date, which combined with extremely deep, near-IR *HST*/NICMOS, and *Spitzer* (3.6, 4.5 μm) datasets form part of the Great Observatories Origins Deep Sur-

vey (GOODS). The depth of the images in this field provides a means to explore high-redshift galaxies to a relatively low limiting stellar-mass. Here, we focus on a sample of galaxies selected with red $J_{110} - H_{160}$ colors in an effort to identify candidates for passively evolving galaxies at $z \gtrsim 2$. Similarly, Brammer & van Dokkum (2007) use a $\tilde{J} - H$ color selection to identify red galaxies at $z > 2$ using the deep FIRES near-IR survey imaging. The *HST*/NICMOS data for the HUDF allow us to probe objects with lower stellar masses than has been previously possible. For example, Dickinson et al. (2000) used deep NICMOS data in the *Hubble* Deep Field (HDF; Williams et al. 1996) to study an unusually red ($J_{110} - H_{160} \gtrsim 2$ mag) source, possibly a passively evolving $z \sim 3$ galaxy with $M > 3 \times 10^{10} M_{\odot}$. Similarly, Chen & Marzke (2004) used the HUDF *HST* images to identify red galaxies ($i_{775} - H_{160} > 2$) with photometric redshifts $z_{\text{ph}} > 2.8$ (see also Yan et al. 2004). In this work we use the HUDF data to study the number density and mass density of objects at $2.5 < z < 3.5$ with colors consistent with older passively evolving stellar populations. To study the HUDF $J_{110} - H_{160} > 1$ sources, when possible we include GOODS IRAC 3.6-4.5 μm and MIPS 24 μm data, which allows us to better constrain the nature of the stellar populations in these objects (as we discuss below).

Throughout this paper we assume the following cosmological parameters: $\Omega_M = 0.3$, $\Omega_{\Lambda} = 0.7$ and $H_0 = 70 \text{ km s}^{-1} \text{ Mpc}^{-1}$ (consistent with the latest *WMAP* results, e.g., Spergel et al. 2003). We use $B_{435}V_{606}i_{775}z_{850}J_{110}H_{160}$ to denote magnitudes derived in the the *HST* ACS and NICMOS bandpasses F435W, F606W, F775W, F850LP, F110W and F160W respectively. We denote magnitudes derived from the IRAC channel 1 and channel 2 data as [3.6 μm] and [4.5 μm]. For reference, the effective wavelengths of these bandpasses are 0.43, 0.60, 0.77, 0.91, 1.1, 1.6, 3.6 and 4.5 μm . All magnitudes henceforth are on the AB system, $m(\text{AB}) = 23.9 - 2.5 \log(f_{\nu}/1 \mu\text{Jy})$.

2. RED GALAXIES IN THE HUDF: PHOTOMETRY AND SELECTION

We combine *HST*/ACS and NICMOS observations of the HUDF (Beckwith et al. 2006³; Thompson et al. 2005) over a $2.4 \times 2.4 \text{ arcmin}^2$ area with *Spitzer* IRAC observations from GOODS (M. Dickinson et al., in preparation)⁴. The plate scale of the drizzled images is 0.03, 0.09 and 0.6 arcsec pix⁻¹ for the ACS, NICMOS, and IRAC data respectively. The 10σ AB point source detection limits for the ACS and NICMOS images are 29.2, 30.0, 29.7, 28.7, 27.0 and 27.0 mag for the $B_{435}V_{606}i_{775}z_{850}J_{110}H_{160}$ images respectively. For the IRAC bands, the 5σ AB point source detection limits are 26.3 mag (0.11 μJy) and 25.6 mag (0.2 μJy), for [3.6 μm] and [4.5 μm] (M. Dickinson, private communication, 2005).

We use ACS images reprocessed by Thompson et al. (2005) and matched to the NICMOS plate-scale and orientation. We then convolve the ACS images by a kernel to match the point spread function (PSF) of the H_{160} -band image. Because the PSFs of the J_{110} and H_{160} images are similar we do not convolve the J_{110} -band image.

³ <http://www.stsci.edu/hst/udf>

⁴ <http://www.stsci.edu/science/goods/>

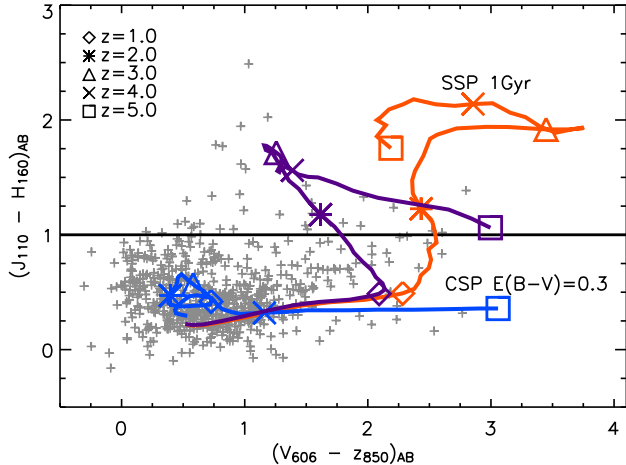


FIG. 1.— Color-color plot of all catalog objects with $H_{160} < 26.0$. The $J_{110} - H_{160} > 1.0$ color cut is marked. The color evolution of three Bruzual & Charlot (2003) models is shown, with integer red-shift steps marked. The curve labeled SSP (orange) is a 1.0 Gyr old simple stellar population formed in a burst with no subsequent star formation. The CSP curve (blue) is a 100 Myr constant star-forming model attenuated using Calzetti et al. (2000) dust. The purple curve is a superposition of these two SSP and CSP models, with a ratio (SSP:CSP) of 99 : 1 by mass. Although the SSP and CSP models do not individually characterize the data well, the two-component model does. The median error for the $J_{110} - H_{160}$ color is smaller than the symbol size; the median error for the $V_{606} - z_{850}$ color is similar to the symbol size.

We use standard IRAF packages to perform the image convolution. Our tests show that point-source photometry on the convolved images recovers the same fraction of the total flux to within 5% for aperture radii greater than 5 pixels (0.45 arcsec). Source detection was executed using the SExtractor software (v2.3.2, Bertin & Arnouts 1996) on a summed $J_{110} + H_{160}$ image, and photometry was performed on the individual PSF-matched images. We use the same detection and photometry parameters as in Thompson et al. (2005). We restrict our analysis to objects with $H_{160} < 26$ mag measured in the SExtractor elliptical, quasi-total (“Kron”; SExtractor MAG_AUTO) apertures. The NICMOS data detect galaxies to 27th magnitude, and adopting a $H_{160} < 26$ mag limit ensures that we can derive robust colors for objects with $J_{110} - H_{160} = 1$. We measure ACS and NICMOS colors for objects in the PSF-matched images using isophotal (MAG_ISO) apertures derived from the H_{160} -image; we correct the isophotal magnitudes to total magnitudes using the difference between the H_{160} -band MAG_AUTO and MAG_ISO magnitudes.

The photometric errors from SExtractor are underestimated because they do not take into account pixel-to-pixel correlations from, for example, the drizzling and PSF-convolution processes. We therefore estimate photometric errors from the binned, drizzled, PSF-convolved ACS images themselves. We measure the sky noise as a function of aperture size in blank regions of each image. We then parameterize the noise as a power law, $\sigma = A \times n_{\text{pix}}^{\beta}$, where σ is the noise measured in an aperture with a size of n_{pix} pixels, and we fit for β and A . In order to measure the noise in the convolved images we tabulate 1250 randomly positioned aperture

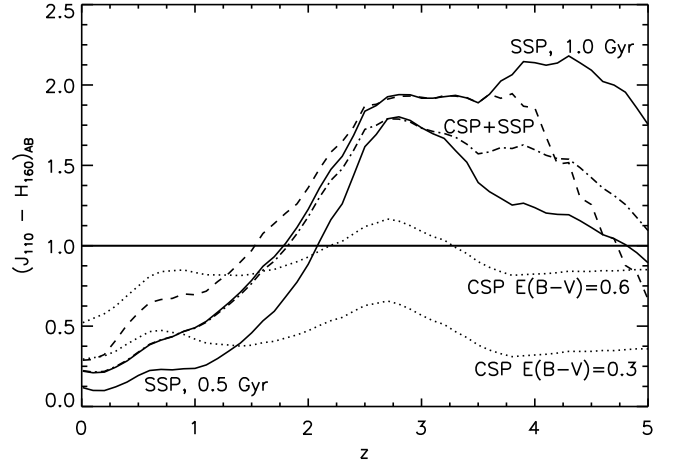


FIG. 2.— Color vs. redshift diagram of Bruzual & Charlot (2003) population synthesis models showing $J_{110} - H_{160}$ color evolution for different ages, star-formation histories and dust attenuations. The solid curves show a simple stellar population (SSP) model at two different ages (1.0 Gyr and 0.5 Gyr). The dotted curves show a 100 Myr constant star-formation model (composite stellar population: CSP) with two different dust attenuations: $E(B - V) = 0.3$ (lower dotted curve) and $E(B - V) = 0.6$ (upper dotted curve). The dot-dashed curve (labeled SSP+CSP) shows an example of a two-component model: an old population (1.0 Gyr SSP) and a young population (100 Myr constant star-formation with $E(B - V) = 0.3$) are combined with a ratio (SSP:CSP) of 99 : 1 by mass. The dashed curve shows a maximally old SSP formed at $z = 7$. Note that our selection criterion, $J_{110} - H_{160} > 1.0$, generally excludes objects at redshifts less than $z \sim 1.5$.

fluxes; we then bin these data and fit for the width of the distribution with a Gaussian function. We exclude bins in the non-Gaussian positive tail of the distribution (these correspond to apertures that receive some flux from bonafide sources in the image). This procedure is repeated for 11 aperture diameters in each band: 0.54, 0.60, 0.80, 0.99, 1.15, 1.30, 1.40, 1.53, 1.65, 1.80 and 2.25. We obtain best-fit values of $\beta = 0.74, 0.92, 0.96, 0.93$ and $A = (5.6, 3.5, 2.0, 2.2) \times 10^{-4}$ ADU sec^{-1} , for $B_{435}V_{606}i_{775}z_{850}$ respectively. Using these fitted values, we can then derive the error, σ in each band for any isophotal aperture size, n_{pix} .

In figure 1 we plot the $J_{110} - H_{160}$ vs. $V_{606} - z_{850}$ colors for all $H_{160} < 26.0$ catalog objects. We also show the color evolution of three Bruzual & Charlot (2003) models, a passively evolving burst (SSP) model, a constant star-forming (CSP) model, and a composite SSP+CSP model, at fixed age and as a function of redshift. The composite model characterizes the $J_{110} - H_{160} > 1$ selected objects well.

To target galaxies whose light is dominated by evolved stellar populations, we select objects with $J_{110} - H_{160} > 1.0$ mag and $H_{160} \leq 26$ mag, which in principle selects objects with a prominent 4000 Å/Balmer break at $z \gtrsim 1.5$. In figure 2 we plot several fiducial stellar population synthesis models from Bruzual & Charlot (2003), with solar metallicity and a Salpeter IMF. Our color criterion excludes model stellar populations with recent star formation (and low-to-moderate dust attenuations), and should be sensitive to passively evolving, older, simple stellar populations (SSPs), or dust-enshrouded objects with younger stellar populations. We find 32 objects satisfying $J_{110} - H_{160} > 1.0$ mag and $H_{160} \leq 26.0$ mag in

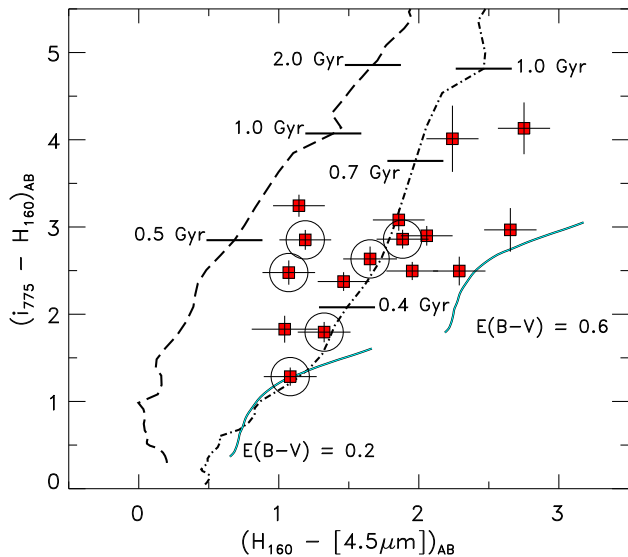


FIG. 3.— $H_{160} - [4.5\mu\text{m}]$ versus $i_{775} - H_{160}$ colors for the 16 galaxies in the $J_{110} - H_{160} > 1$ mag sample with robust IRAC photometry. The lines show colors of various model stellar populations formed at $z = 7$. The dashed line shows the expected colors of a passively evolving stellar population observed at $z = 2.7$, formed in a burst as a function of age, t ; the dot-dashed line shows the same model observed at $z = 3.5$. Tick marks denote the model ages along the dashed and dot-dashed curves as labeled. The solid lines show colors of a stellar population with constant star formation formed at $z = 7$ as a function of age and extinction with color excess $E(B - V) = 0.2$ and 0.6 , as labeled. The encircled data points indicate the 6 candidates for distant galaxies dominated by old stellar populations (see § 4.1). These models roughly bound the galaxy colors, and indicate that including the IRAC data we can understand the properties of the stellar populations in these galaxies. Note that none of the objects have colors consistent with passively evolving stellar populations older than 1 Gyr.

the NICMOS-selected catalog; their properties are summarized in table 1.

We match $J_{110} - H_{160} > 1$ mag objects against the *Spitzer*/IRAC catalog from the Great Observatories Origins Deep Survey (GOODS; M. Dickinson et al. in preparation). Source detection for this catalog was performed on a summed $[3.6\mu\text{m}] + [4.5\mu\text{m}]$ image, and photometry was measured in circular, $4.0''$ -diameter apertures, which we correct to total magnitudes by adding -0.36 and -0.31 respectively to the $[3.6\mu\text{m}]$ and $[4.5\mu\text{m}]$ magnitudes (appropriate for GOODS, M. Dickinson et al., in prep, and slightly larger than those in the IRAC data handbook⁵). Because the image PSF size is substantially different between the NICMOS and IRAC images (FWHM $0''.3$ and $1''.6$, respectively), we do not attempt to PSF match these images.

We matched these objects to sources in the *Spitzer*/IRAC catalog first using a $4''$ -radius criterion. We then visually inspected each source and accept only those objects whose positions coincide with the *HST* source (they are well-centered) and who are isolated (unblended) from other *HST* sources within that radius. This is a conservative approach, and has the advantage of limiting our analysis to only those *Spitzer* counterparts that are free from source confusion. Of the 32 objects in the parent sample, 16 have unblended IRAC $[3.6\mu\text{m}]$ and $[4.5\mu\text{m}]$ counterparts. In figures 5-8 we show the

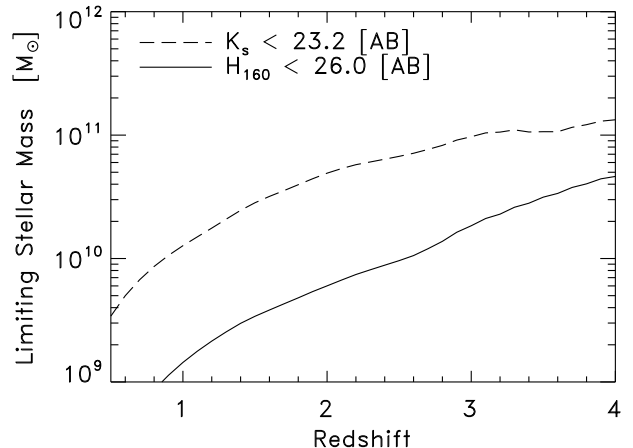


FIG. 4.— Limiting stellar mass for galaxies with a stellar population formed in a burst at $z = 7$ with observed magnitude $H_{160} = 26.0$ or $K_s = 23.2$. The HUDF data are sensitive to passively evolving stellar populations with masses above these limits.

ACS, NICMOS, and IRAC images and spectral energy distributions (SEDs) of these objects.

Including the IRAC data extends our wavelength coverage, allowing us to discriminate broadly between galaxies dominated by dust-obscured starbursts and galaxies with a substantial amount of stellar mass in later-type stars (see, e.g., Labbé et al. 2005). In figure 3, we show a $H_{160} - [4.5\mu\text{m}]$ versus $i_{775} - H_{160}$ plot to study the stellar populations and dust extinction properties for the 16 galaxies with IRAC photometry. We also plot fiducial colors of a passively evolving stellar population and dust-enshrouded starbursts (with $E(B - V) = 0.2$ and 0.6 , using the extinction law from Calzetti et al. 2000) as a function of stellar population age at $z = 2.7$. These simple models bound the range of colors observed in the $J_{110} - H_{160} > 1$ mag objects, comparable to findings for red, $J - K_s$ -selected galaxies in other fields (Labbé et al. 2005; Papovich et al. 2006). Blue $H_{160} - [4.5\mu\text{m}]$ colors ($\lesssim 2$ mag) at this redshift (rest-frame $0.4 - 1.2$ micron) result from substantial older stellar populations, which produce a significant Balmer/4000 Å break, causing redder $i_{775} - H_{160}$ colors (and also the red $J_{110} - H_{160}$ color that satisfy the selection criteria). Objects at these redshifts with redder $H_{160} - [4.5\mu\text{m}]$ colors ($\gtrsim 2$ mag) require dust-enshrouded, ongoing star formation. The galaxies with $J_{110} - H_{160} > 1$ and IRAC photometry all have a similar range of $i_{775} - H_{160}$ colors, making it difficult to differentiate between the two types of stellar populations. However, these galaxies span a large range in $H_{160} - [4.5\mu\text{m}]$ colors, from 1-4 mag. Many of the objects appear to have colors consistent with dust-enshrouded, young stellar populations, while a few sources have colors consistent with a substantial amount of their stellar mass in older stars. Based on figure 3, there are few galaxies whose colors are consistent with a pure passively evolving, older stellar population. We discuss this further in § 4.

We also include other multiwavelength data to interpret the nature of the $J_{110} - H_{160} > 1$ mag sample. In particular, we use *Spitzer*/MIPS $24\mu\text{m}$ data for this field from the catalog of Papovich et al. (2004). These data al-

⁵ <http://ssc.spitzer.caltech.edu/irac/dh/>

TABLE 1
PHOTOMETRIC PROPERTIES OF THE NICMOS-UDF J₁₁₀ - H₁₆₀ > 1.0 SAMPLE

NIC ID	R.A. [J2000]	Decl. [J2000]	z_{tot} AB	H_{tot} AB	$B - z$ AB	$V - z$ AB	$I - z$ AB	$z - H$ AB	$J - H$ AB	[3.6 μ m] AB	[4.5 μ m] AB	Alternate ID
30*	03:32:39.72	-27:46:11.3	23.60	21.73	1.55	1.28	0.63	1.87	1.18	19.96	19.77	1 ^c
66	03:32:39.32	-27:46:23.6	25.41	24.00	1.48	0.64	0.32	1.41	1.10
86	03:32:37.13	-27:46:25.9	24.99	23.23	5.41	2.60	1.03	1.76	1.02	2 ^c
88*	03:32:38.01	-27:46:26.3	25.68	23.30	2.27	1.50	0.71	2.37	1.43	21.59	21.44	3 ^c
99	03:32:36.17	-27:46:27.7	24.58	23.07	1.47	0.80	0.45	1.51	1.05
111*	03:32:41.75	-27:46:28.9	27.12	25.53	1.22	0.99	0.24	1.59	1.21	24.44	24.48	...
120*	03:32:41.01	-27:46:31.5	26.57	24.50	1.53	0.96	0.42	2.07	1.35	22.42	22.21	...
215	03:32:34.77	-27:46:46.1	26.41	25.08	1.61	0.91	0.23	1.33	1.05
219*	03:32:43.32	-27:46:46.9	26.16	23.76	1.79	0.76	0.24	2.39	1.78	22.21	22.11	9151 ^a
223*	03:32:35.06	-27:46:47.6	25.79	23.36	1.97	0.97	0.43	2.43	1.62	21.61	21.48	9024 ^a , 4 ^c , 8 ^d
234	03:32:42.96	-27:46:49.9	23.43	21.81	4.29	2.52	0.90	1.62	1.03
245	03:32:39.88	-27:46:50.0	26.67	25.71	0.07	0.20	0.04	0.97	1.03
269*	03:32:38.73	-27:46:54.1	25.74	24.63	1.11	0.45	0.18	1.10	1.09	23.28	23.55	...
281	03:32:41.67	-27:46:55.4	26.03	23.72	2.05	1.54	0.97	2.31	1.28
319*	03:32:34.42	-27:46:59.7	24.28	22.31	3.03	2.21	0.93	1.97	1.24	20.40	20.25	5 ^c
478	03:32:42.52	-27:47:14.3	26.14	24.75	1.77	0.52	0.04	1.39	1.12
535	03:32:34.62	-27:47:20.9	25.00	23.38	2.38	1.94	0.84	1.61	1.08
625*	03:32:43.46	-27:47:27.4	26.63	24.34	2.63	0.82	0.18	2.29	1.77	23.18	23.26	6140 ^a
683	03:32:36.96	-27:47:27.2	25.22	23.23	2.33	1.49	0.62	1.99	1.08
706*	03:32:42.73	-27:47:33.9	24.37	22.74	1.90	1.51	0.75	1.63	1.05	21.28	21.27	5256 ^a
902	03:32:38.10	-27:47:49.8	24.47	22.17	3.82	1.80	0.93	2.30	1.10	3650 ^b
921*	03:32:39.11	-27:47:51.6	25.50	23.11	3.36	1.55	0.86	2.39	1.19	21.92	21.96	3574 ^b , 13 ^d
935	03:32:33.26	-27:47:52.4	27.23	24.77	2.05	1.97	0.98	2.46	1.33	6 ^d
989*	03:32:34.93	-27:47:56.0	26.21	24.76	1.70	0.57	0.35	1.44	1.06	23.37	23.44	...
1078*	03:32:42.87	-27:48:09.5	28.06	24.54	2.02	1.03	0.62	3.51	2.49	22.03	21.78	12182 ^a , 1 ^d
1082	03:32:38.70	-27:48:10.3	27.35	25.84	1.75	0.73	0.09	1.51	1.34
1172*	03:32:41.74	-27:48:24.9	27.75	24.56	2.02	2.80	0.83	3.18	1.39	22.48	22.32	4 ^d
1184	03:32:38.75	-27:48:27.1	26.43	24.57	1.84	0.53	0.17	1.86	1.30	15 ^d
1211*	03:32:39.16	-27:48:32.4	25.78	23.25	2.30	1.19	0.33	2.52	2.02	22.08	22.06	1927 ^a , 1446 ^b , 6 ^c , 9 ^d
1237*	03:32:38.73	-27:48:39.9	27.07	24.48	2.37	0.97	0.38	2.59	1.95	22.03	21.82	12183 ^a , 2 ^d
1245	03:32:39.58	-27:48:42.2	26.21	25.25	1.49	0.59	0.15	0.95	1.07
1267	03:32:39.66	-27:48:50.6	24.36	22.38	2.96	1.01	0.22	1.98	1.57	1223 ^a

NOTE. — Objects with unblended IRAC photometry are marked with *. References for the alternate ID's listed are (a) Chen & Marzke (2004), (b) Daddi et al. (2005), (c) Toft et al. (2005) and (d) Yan et al. (2004a).

low us to test for the emission from dust associated with either star formation or obscured AGN in these galaxies. We also include *Chandra* X-ray data from the catalog of Alexander et al. (2003). At the redshifts of interest for our sample, the X-ray data are sensitive accretion of material onto supermassive blackholes, and thus allow us to test for the presence of AGN in our sample.

3. SED FITTING: MASS ESTIMATES FROM A SIMPLE PHOTOMETRIC REDSHIFT CODE

3.1. Fitting method

To study the properties of our selected objects, we fit stellar-population synthesis models to the photometry and derive redshifts and stellar masses. We model the galaxies as the sum of two stellar components, young and old, and consider the effects of reddening. Because the star-formation history is constrained generally poorly by SED fitting, and the stellar population age and dust extinction have strong degeneracies (see, e.g., Papovich et al. 2001), we consider only non-negative linear superpositions of these two models. The combinations of these two models encompass the range of plausible star-formation histories, and in particular, as we discuss below, they allow us to derive a stringent upper limit on the amount of stellar mass in old stellar populations.

We therefore have four model parameters: the redshift, dust extinction, mass in the young stellar component, and the mass in the older stellar component. We use the Bruzual & Charlot (2003) population synthesis code

to generate the two stellar population components for our SED fitting routine: a 100 Myr constant star formation (composite stellar population: CSP) model and a maximally old passively evolving (simple stellar population: SSP) model formed at $z = 7$, both generated at solar metallicity and with a Salpeter initial mass function (IMF). Our maximally old model age is a function of redshift: the age at a given redshift is equal to the age of the universe at that redshift minus 0.75 Gyr, the age of the universe at $z = 7$. We attenuate the CSP model using the Calzetti et al. (2000) dust law; the old model is not attenuated. At each z and $E(B - V)$, we compute model photometry by convolving the Bruzual & Charlot (2003) spectra with the 8 filter response curves (e.g., Papovich et al. 2001), taking in to account the HI opacity of the intergalactic medium (IGM) along the line of sight (Madau 1995), according the models described in Fan (1999).

We fit the object fluxes to this four-parameter model assuming that the errors in the fluxes are symmetric and Gaussian. In addition to the photometric uncertainties on the magnitude of each bandpass, we add a systematic uncertainty proportional to the flux density of $\sigma_{\text{sys}}/f_{\nu} = 0.04, 0.08$, and 0.15 for the ACS, NICMOS, and IRAC photometry, respectively. These errors represent systematic uncertainties in our matched-band photometry, as well as the fact that our model does not sample the full range of possible parameters infinitesimally.

TABLE 2
BEST-FIT PARAMETERS WITH HST DATA ONLY

NIC ID	z_{phot}	E(B-V) ^a	log M_o/M_\odot ^b	log M_y/M_\odot ^c	f_{old} ^d	$\chi^2_{\nu, best}$ ^e	$\Delta\chi^2$ ^f
30*	$1.4^{+0.2}_{-0.1}$	0.2 ± 0.1	11.2 ± 0.1	$9.0^{+0.5}_{-0.3}$	$0.993^{+0.004}_{-0.010}$	5.2	0.0
66	2.6 ± 0.2	$0.3^{+0.1}_{-0.0}$	$10.6^{+0.1}_{-0.4}$	$9.6^{+0.2}_{-0.1}$	$0.915^{+0.021}_{-0.207}$	2.5	0.3
86	$1.1^{+3.3}_{-0.1}$	$1.1^{+0.3}_{-0.8}$	$10.3^{+1.5}_{-0.2}$	$9.8^{+0.3}_{-0.5}$	$0.763^{+0.224}_{-0.136}$	0.0	0.8
88*	$2.2^{+0.1}_{-0.2}$	0.6 ± 0.1	$10.8^{+0.1}_{-0.2}$	10.0 ± 0.4	$0.867^{+0.083}_{-0.231}$	0.7	0.0
99	2.1 ± 0.1	0.4 ± 0.0	10.7 ± 0.1	$10. \pm 0.1$	$0.857^{+0.018}_{-0.023}$	3.0	0.0
111*	$0.7^{+0.1}_{-0.0}$	$0.0^{+0.1}_{-0.0}$	8.8 ± 0.0	$6.5^{+0.3}_{-0.0}$	$0.996^{+0.000}_{-0.005}$	17.9	0.0
120*	$2.4^{+0.3}_{-0.2}$	0.4 ± 0.1	$10.5^{+0.2}_{-0.1}$	$9.2^{+0.3}_{-0.4}$	$0.948^{+0.032}_{-0.085}$	0.4	0.0
215	0.6 ± 0.0	0.5 ± 0.0	$6.6^{+0.3}_{-0.7}$	7.9 ± 0.0	$0.048^{+0.051}_{-0.034}$	12.6	0.0
219*	2.8 ± 0.1	0.3 ± 0.0	11.0 ± 0.1	$9.3^{+0.0}_{-0.1}$	$0.981^{+0.004}_{-0.002}$	3.5	0.0
223*	$2.9^{+0.3}_{-0.4}$	0.3 ± 0.1	$11.3^{+0.2}_{-0.3}$	$9.4^{+0.2}_{-0.3}$	$0.986^{+0.009}_{-0.027}$	1.3	1.1
234	$0.9^{+0.1}_{-0.0}$	$1.1^{+0.2}_{-0.1}$	10.6 ± 0.1	10.1 ± 0.2	$0.783^{+0.094}_{-0.076}$	1.8	0.0
245	2.4 ± 0.1	0.0 ± 0.0	$10. \pm 0.0$	8.1 ± 0.0	0.989 ± 0.001	14.7	0.0
269*	$2.7^{+0.3}_{-0.1}$	$0.2^{+0.0}_{-0.1}$	$10.4^{+0.3}_{-0.1}$	$9.2^{+0.0}_{-0.2}$	$0.941^{+0.043}_{-0.020}$	2.3	0.0
281	$1.9^{+0.2}_{-0.1}$	$0.3^{+0.2}_{-0.1}$	10.7 ± 0.1	$8.7^{+0.6}_{-0.5}$	$0.992^{+0.005}_{-0.029}$	0.6	0.0
319*	1.1 ± 0.1	$0.9^{+0.1}_{-0.0}$	$10.1^{+0.3}_{-0.5}$	10.2 ± 0.2	$0.421^{+0.218}_{-0.200}$	1.9	0.0
478	3.1 ± 0.2	$0.2^{+0.1}_{-0.0}$	$10.7^{+0.1}_{-0.3}$	$9.2^{+0.2}_{-0.1}$	$0.968^{+0.007}_{-0.086}$	3.1	2.5
535	1.1 ± 0.1	$0.7^{+0.1}_{-0.5}$	$10.0^{+0.3}_{-0.5}$	$9.3^{+0.3}_{-1.5}$	$0.788^{+0.208}_{-0.330}$	4.4	0.0
625*	3.3 ± 0.4	0.2 ± 0.1	$11.1^{+0.2}_{-0.3}$	8.9 ± 0.4	$0.993^{+0.005}_{-0.017}$	3.9	0.0
683	$1.6^{+0.2}_{-0.1}$	0.6 ± 0.1	$10.5^{+0.2}_{-0.3}$	$9.9^{+0.3}_{-0.5}$	$0.800^{+0.139}_{-0.291}$	0.6	0.0
706*	$1.2^{+0.1}_{-0.0}$	$0.3^{+0.1}_{-0.2}$	10.6 ± 0.1	$8.7^{+0.4}_{-0.6}$	$0.988^{+0.009}_{-0.022}$	3.5	0.7
902	1.9 ± 0.1	0.8 ± 0.1	$11.1^{+0.1}_{-0.3}$	$10.8^{+0.2}_{-0.4}$	$0.682^{+0.183}_{-0.295}$	2.8	0.0
921*	$2.0^{+0.1}_{-0.2}$	0.7 ± 0.1	$10.8^{+0.1}_{-0.3}$	$10.2^{+0.4}_{-0.5}$	$0.811^{+0.124}_{-0.306}$	1.3	0.0
935	1.9 ± 0.2	0.5 ± 0.4	$10.3^{+0.1}_{-0.3}$	8.6 ± 1.2	$0.978^{+0.021}_{-0.445}$	0.9	0.7
989*	3.1 ± 0.3	0.2 ± 0.1	$10.7^{+0.2}_{-0.3}$	9.1 ± 0.3	$0.979^{+0.014}_{-0.049}$	1.6	0.1
1078*	$2.9^{+0.3}_{-0.2}$	0.1 ± 0.1	10.8 ± 0.2	$7.5^{+0.6}_{-0.4}$	$1.000^{+0.000}_{-0.001}$	6.6	0.6
1082	$2.7^{+0.0}_{-0.1}$	0.4 ± 0.0	$9.6^{+0.1}_{-0.2}$	9.2 ± 0.0	$0.707^{+0.062}_{-0.112}$	6.0	0.0
1172*	2.0 ± 0.4	$1.1^{+0.3}_{-0.8}$	$10.4^{+0.2}_{-0.6}$	$10.1^{+0.6}_{-2.3}$	$0.513^{+0.485}_{-0.397}$	1.0	0.8
1184	$3.2^{+0.2}_{-0.3}$	0.2 ± 0.1	10.9 ± 0.2	9.0 ± 0.3	$0.987^{+0.009}_{-0.029}$	0.4	0.2
1211*	$2.9^{+0.4}_{-0.2}$	0.4 ± 0.1	$11.2^{+0.3}_{-0.2}$	9.8 ± 0.3	$0.960^{+0.028}_{-0.081}$	9.5	1.0
1237*	$3.3^{+0.3}_{-0.4}$	$0.1^{+0.2}_{-0.1}$	11.0 ± 0.2	$8.3^{+0.5}_{-0.4}$	$0.998^{+0.001}_{-0.008}$	2.7	0.0
1245	$2.8^{+0.3}_{-0.1}$	$0.3^{+0.0}_{-0.1}$	9.8 ± 0.5	$9.3^{+0.1}_{-0.2}$	$0.766^{+0.182}_{-0.260}$	5.6	1.7
1267	$3.2^{+0.2}_{-0.3}$	0.4 ± 0.1	$11.6^{+0.2}_{-0.3}$	10.6 ± 0.3	$0.921^{+0.054}_{-0.180}$	5.1	0.0

NOTE. — Columns 2 through 4 list the median values and the 16% and 82% intervals for the fitted parameters. Objects with unblended IRAC photometry are marked with an asterisk symbol. Objects 30, 88, 1237 and 1267 are detected in x-rays.

^a The E(B-V) extinction is applied only to the young component

^b The model fit mass in the old (SSP) component.

^c The model fit mass in the young (constant SFR) component.

^d The fraction by mass of the old component relative to the total fitted mass.

^e The best-fit model χ^2_ν is listed.

^f The difference between the χ^2 value for the model listed in columns 2 through 4 and the best χ^2 :

$\Delta\chi^2 = \chi^2_{median} - \chi^2_{best}$ (also see Section 3.1).

These systematic errors are added in quadrature to either the fitted errors, for the ACS photometry, or the catalog errors for the NICMOS and IRAC photometry. We use the resulting χ^2 statistic to produce the likelihood $\mathcal{L} \propto \exp(-\chi^2/2)$ and we take the likelihood to be the probability distribution for the 4 parameters given the observed fluxes.

We derive mean values and variances for the 4 parameters (and functions thereof) by integrating over the full 4-dimensional likelihood. The integrations are done with a hybrid grid plus Monte Carlo approach. The χ^2 is quadratic in two parameters (the old and young masses, M_o and M_y) and more complicated in the other two (redshift and reddening). We construct a grid in redshift and reddening over the range $0 < z < 5$ and $0 < E(B - V) < 1.5$. For each point, we use linear methods to find the best fit and Gaussian covariance ma-

trix for the masses. We generate Gaussian-distributed points given this covariance region and weight points by $\exp(-\chi^2_{best}/2)$ for the best-fit χ^2 , dropping any points that have negative masses. The concatenation of all of the points is a Monte Carlo of the full 4-dimensional likelihood, and any function can be computed by a simple weighted sum of the function evaluated at all of the points. Similarly, we can construct quantiles by sorting the points according to a given function evaluation and cumulating the weights. By using a grid in the non-quadratic directions, we ensure that multiple minima are found and correctly weighted.

The derived physical parameters are presented in table 2 and table 3. In these tables we define f_{old} to be the ratio of the mass in the passively evolving component, M_o to the total mass, $M_o + M_y$, where M_y is the mass

TABLE 3
BEST-FIT PARAMETERS FOR OBJECTS WITH IRAC PHOTOMETRY

NIC ID	z_{phot}	$E(B-V)^a$	$\log M_o/M_\odot^b$	$\log M_y/M_\odot^c$	f_{old}^d	$\chi_\nu^2{}^e$	$\Delta\chi^2{}^f$
30**	$1.8^{+0.2}_{-0.1}$	$0.3^{+0.1}_{-0.0}$	11.5 ± 0.1	$9.7^{+0.5}_{-0.1}$	$0.984^{+0.002}_{-0.026}$	9.2	0.0
88**	$2.2^{+0.2}_{-0.1}$	$0.7^{+0.0}_{-0.1}$	10.8 ± 0.2	$10.3^{+0.1}_{-0.2}$	$0.718^{+0.158}_{-0.071}$	0.7	0.0
111	$1.5^{+0.1}_{-0.0}$	0.4 ± 0.0	9.6 ± 0.1	$8.5^{+0.1}_{-0.0}$	$0.914^{+0.010}_{-0.015}$	11.3	0.0
120**	$3.4^{+0.1}_{-0.2}$	0.2 ± 0.1	11.1 ± 0.1	8.9 ± 0.4	$0.994^{+0.004}_{-0.012}$	2.0	0.2
219★	$2.8^{+0.2}_{-0.0}$	$0.3^{+0.0}_{-0.1}$	11.1 ± 0.1	$9.3^{+0.0}_{-0.3}$	$0.982^{+0.011}_{-0.002}$	2.2	0.0
223★	3.1 ± 0.1	$0.2^{+0.1}_{-0.0}$	11.4 ± 0.1	$9.1^{+0.0}_{-0.0}$	$0.995^{+0.000}_{-0.007}$	0.7	0.0
269★	$2.7^{+0.1}_{-0.0}$	0.2 ± 0.0	10.4 ± 0.1	9.2 ± 0.0	$0.944^{+0.007}_{-0.008}$	1.9	0.0
319**	$1.2^{+0.0}_{-0.1}$	$0.9^{+0.1}_{-0.0}$	$10.0^{+0.2}_{-0.4}$	10.3 ± 0.1	$0.344^{+0.129}_{-0.156}$	1.3	0.0
625★	2.7 ± 0.1	$0.4^{+0.0}_{-0.1}$	10.6 ± 0.1	$9.4^{+0.1}_{-0.3}$	$0.937^{+0.039}_{-0.015}$	3.3	0.0
706	$1.3^{+0.2}_{-0.0}$	0.6 ± 0.0	$10.3^{+0.2}_{-0.3}$	9.9 ± 0.1	$0.703^{+0.095}_{-0.137}$	4.2	0.0
921	1.9 ± 0.1	0.5 ± 0.1	10.9 ± 0.1	9.5 ± 0.3	$0.966^{+0.019}_{-0.045}$	1.6	0.0
989★	$2.9^{+0.1}_{-0.2}$	$0.3^{+0.0}_{-0.1}$	$10.5^{+0.2}_{-0.1}$	$9.3^{+0.1}_{-0.3}$	$0.935^{+0.042}_{-0.019}$	1.3	1.5
1078	$2.9^{+0.7}_{-0.3}$	$1.0^{+0.0}_{-1.0}$	$10.6^{+0.6}_{-0.3}$	$10.7^{+0.1}_{-3.3}$	$0.386^{+0.614}_{-0.123}$	5.8	2.4
1172	$2.1^{+0.2}_{-0.3}$	$1.1^{+0.3}_{-0.1}$	$10.4^{+0.1}_{-0.2}$	$10.1^{+0.1}_{-0.2}$	$0.661^{+0.078}_{-0.072}$	1.0	0.3
1211★	2.7 ± 0.1	$0.4^{+0.1}_{-0.0}$	11.0 ± 0.1	9.9 ± 0.2	$0.949^{+0.013}_{-0.073}$	5.0	0.5
1237**	$3.6^{+0.2}_{-0.0}$	$0.0^{+0.1}_{-0.0}$	$11.2^{+0.1}_{-0.0}$	$8.0^{+0.4}_{-0.1}$	$0.999^{+0.000}_{-0.001}$	1.9	0.0

NOTE. — Columns 2 through 4 list the median values and the 16% and 82% intervals for the fitted parameters. The six galaxies with broad-band SEDs consistent with distant evolved stellar populations are marked with a star symbol. Objects detected at $24\mu\text{m}$ are indicated with a double-asterisk symbol. Objects 30, 88, and 1237 are detected in x-rays.

^a The $E(B-V)$ extinction is applied only to the young component

^b The model fit mass in the old (SSP) component.

^c The model fit mass in the young (constant SFR) component.

^d The fraction by mass of the old component relative to the total fitted mass.

^e The best-fit model χ_ν^2 is listed.

^f The difference between the χ^2 value for the model listed in columns 2 through 4 and the best χ^2 : $\Delta\chi^2 = \chi_{\text{median}}^2 - \chi_{\text{best}}^2$ (also see Section 3.1).

in the star-forming component,

$$f_{\text{old}} = M_o / (M_o + M_y). \quad (1)$$

We characterize the probability distribution function for the various parameters by the median and the 16% and 84% intervals (equivalent to the 1σ intervals for a Gaussian distribution). However, in cases with multiple minima these simple quantiles will not fully represent the distribution.

3.2. Fitting results

We apply this SED fitting method to derive physical parameters for our objects. We present the results of the ACS and NICMOS photometry fitting analysis in detail in Table 2 and summarize them here as follows.

The fits to 11 objects in our sample favor models with relatively lower redshifts ($z_{\text{phot}} < 2.5$) and lower stellar mass fractions in old stellar populations ($f_{\text{old}} < 0.9$): NIC IDs 86, 88, 99, 215, 234, 319, 535, 683, 902, 921, and 1172. We note that on average this set of galaxies has more dust, with a mean fitted $E(B-V) \sim 0.8$, than the entire sample, which has a mean fitted $E(B-V) \sim 0.4$. The fits to 7 objects favor models with lower redshifts and higher mass fractions in older stars ($z_{\text{phot}} < 2.5$ and $f_{\text{old}} > 0.9$): 30, 111, 120, 245, 281, 706, and 935. For objects 1082 and 1245, the models favor a solution with high redshift ($z_{\text{phot}} > 2.5$) and a relatively low fraction of mass in old stars ($f_{\text{old}} < 0.9$). For 12 objects the models favor solutions with high redshift ($z_{\text{phot}} > 2.5$) and a relatively high fraction of stars in the old stellar population ($f_{\text{old}} > 0.9$): 66, 219, 223, 269, 478, 625, 989, 1078, 1184, 1211, 1237 and 1267.

We find that when we include the IRAC [$3.6\mu\text{m}$] and [$4.5\mu\text{m}$] data in the model fitting, 12 objects (of the 16 with unblended IRAC photometry) have consistent results compared to the model fits without the IRAC data. Of these 12 objects, 6 objects are fitted with high-redshift model galaxies with only small amounts of rest-frame UV light associated with a young stellar population or on-going star formation (for this set $z_{\text{phot}} \geq 2.7$ and $f_{\text{old}} > 0.93$). The fitted model parameters for these 16 objects are listed in Table 3. Here we discuss the particularities of these objects and their corresponding fits. We will not individually discuss the objects without IRAC photometry. However, we note that object 1267, is detected in the X-ray data, with a $0.5 - 2.0$ keV flux of $f_x = 7.5 \times 10^{-16}$ ergs cm^{-2} s^{-1} .

NIC ID = 30: The difference in the fitted parameters when we include the IRAC data is significant: $\Delta z_{\text{phot}} \sim 0.4$. As expected, the masses change as well. However, both values for f_{old} remain high. The best-fit χ_ν^2 is very large for the IRAC fit ($\chi_\nu^2 = 9.2$). This is due to the large amount of IRAC flux that our models inadequately characterize (see figure 5); this excess is also driving the selection of a higher redshift and mass. Toft et al. (2005) derive a photometric redshift of $z = 2.2$, roughly consistent with our IRAC fit redshift $z = 1.8^{+0.2}_{-0.1}$. However, this object is detected with MIPS at $24\mu\text{m}$ with $f_\nu(24\mu\text{m}) = 190 \mu\text{Jy}$, and it has an X-ray data detection of $f_X(0.5 - 2\text{keV}) = 8.4 \times 10^{-16}$ ergs cm^{-2} s^{-1} . Based on this data it is likely that this object likely has an AGN; therefore we consider the lower redshift fit more plausible. Furthermore, it is possible that the AGN contributes to the broadband photometry, and our model

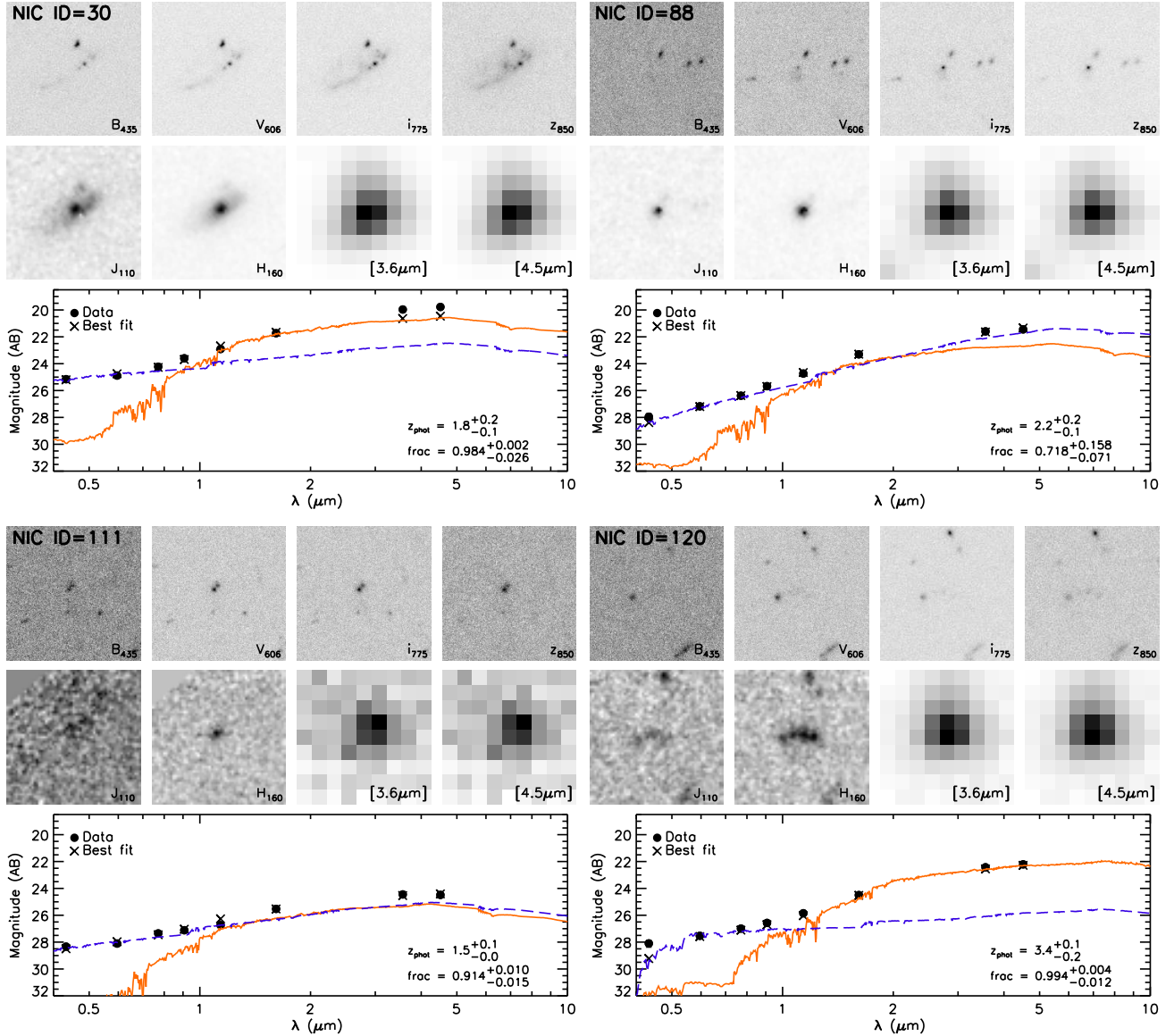


FIG. 5.— Gallery of $J_{110} - H_{160} > 1.0$ and $H_{160} < 26.0$ selected objects; we show imaging, broad-band SED's and the best fit model for each object. The $B_{435}V_{606}i_{775}z_{850}J_{110}H_{160}[3.6\mu m][4.6\mu m]$ postage stamps are $5''.4$ on a side and oriented such that North is up and East is to the left. The $B_{435}V_{606}i_{775}z_{850}J_{110}H_{160}$ stamps are plotted at constant f_ν per arcsec and are displayed on a log scale. The IRAC imaging is also displayed at constant f_ν per arcsec but on a different relative scale than the $B_{435}V_{606}i_{775}z_{850}J_{110}H_{160}$ imaging. The broad-band SED's are shown in the lower panels with solid circles, 1σ error bars are indicated. The crosses indicate the best fit model. The dashed line indicates the fraction, by mass, of light that is attributed by the best fit to the young model; similarly, the solid line indicates the fraction attributed to the old model.

fits may not be valid for this object.

NIC ID = 88: The two fits, with and without the IRAC data, are consistent, with $z_{\text{phot}} \sim 2.2$ and $f_{\text{old}} \sim 0.8$. It is detected at $24\mu m$ with $f_\nu(24\mu m) = 70 \mu Jy$, although inspection of the $24\mu m$ image shows that the object is blended (with a PSF FWHM $\simeq 6''$). This object also has a $0.5 - 2.0$ keV x-ray flux $f_X = 8.8 \times 10^{-16}$ ergs $cm^{-2} s^{-1}$ (Alexander et al. 2003). In conjunction these data indicate that this object is likely host to an AGN, a conclusion that is supported by the fact that this object has red IRAC $[5.8\mu m] - [8.0\mu m]$ colors and that it has a compact morphology in the HST images (see figure 5). As with NIC ID 30, the presence of an AGN may imply that the models are inadequate.

NIC ID = 111: The best-fit model, derived including

the IRAC data, is lower redshift older stellar population: $z_{\text{phot}} = 1.5$ and $f_{\text{old}} = 0.914$. The model derived from the ACS and NICMOS data alone have a similar f_{old} , but the redshift is much lower, $z = 0.7$. This discrepancy is driven by the bright IRAC photometry; our models are simply not red enough at $z = 0.7$ to reproduce the mid-IR data. This indicates that the ACS and NICMOS broad-band photometry alone does not adequately characterize this object.

NIC ID = 120: The fitted photometric redshifts and masses are consistent with a distant old stellar population dominating the flux in the rest-frame optical and a younger stellar population (or on-going star formation) dominating in the rest-frame UV, with $z_{\text{phot}} = 3.4$ and $f_{\text{old}} = 0.994$. The physical parameters derived with-

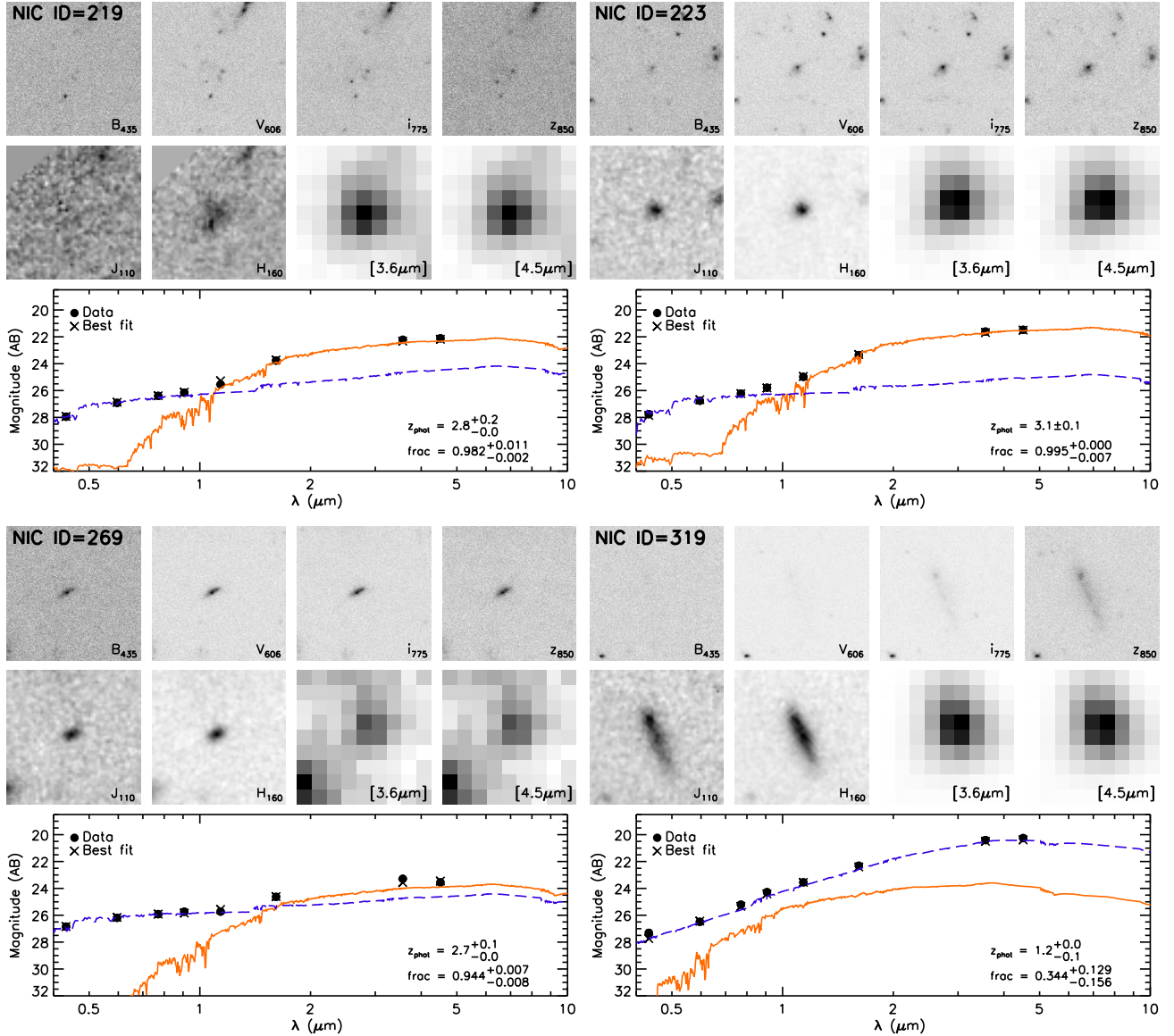


FIG. 6.— Same as figure 5.

out the IRAC data are *not* consistent with this interpretation, with a much smaller distance ($z = 2.4$) and a somewhat lower fraction ($f_{\text{old}} = 0.948$). Inspection of the images reveals that the blue component dominating the rest-frame UV photometry is unresolved and just off-center (see figure 5). Therefore, the possibility that this SED is the result of the projection of more than one object cannot be ruled out. Despite the fact that $[5.8\mu\text{m}]$ and $[8.0\mu\text{m}]$ IRAC fluxes are in good agreement with the distant old population scenario, we do not include this object in our set of distant and evolved object candidates because of the discrepancy between the two model fits. Furthermore, this object is detected at $24\mu\text{m}$.

NIC ID = 219: Our fitted physical parameters are consistent with a high redshift galaxy dominated by an old stellar population ($z_{\text{phot}} = 2.8$ and $f_{\text{old}} = 0.98$). The fit derived from the dataset including IRAC data is consistent with this model. The derived redshift is also consistent with the photometric redshifts of Chen & Marzke

(2004).

NIC ID = 223: The fitted model is a distant galaxy dominated by an old stellar population, with best-fit parameters $z_{\text{phot}} = 3.1 \pm 0.1$ and $f_{\text{old}} = 0.995$, consistent with the model derived from the ACS and NICMOS data alone. Chen & Marzke (2004) derive a photometric redshift of $z_{\text{phot}} = 3.11$, in good agreement with our derived redshift. Yan et al. (2004a) derive a $z_{\text{phot}} = 2.9$ and Toft et al. (2005) derive a $z_{\text{phot}} = 3.4$, however, these authors do not quote errors, making it hard to compare with our model.

NIC ID = 269: The fit parameters are consistent with a distant object dominated by an old stellar population with a small amount of ongoing star formation, for both fits with and without IRAC data ($z_{\text{phot}} = 2.7$ and $f_{\text{old}} = 0.94$).

NIC ID = 319: The most-likely model is a low redshift dusty starburst: $z_{\text{phot}} = 1.2$, $E(B - V) = 0.9$ and $f_{\text{old}} = 0.34$. Toft et al. (2005) derive a $z_{\text{phot}} = 1.8$

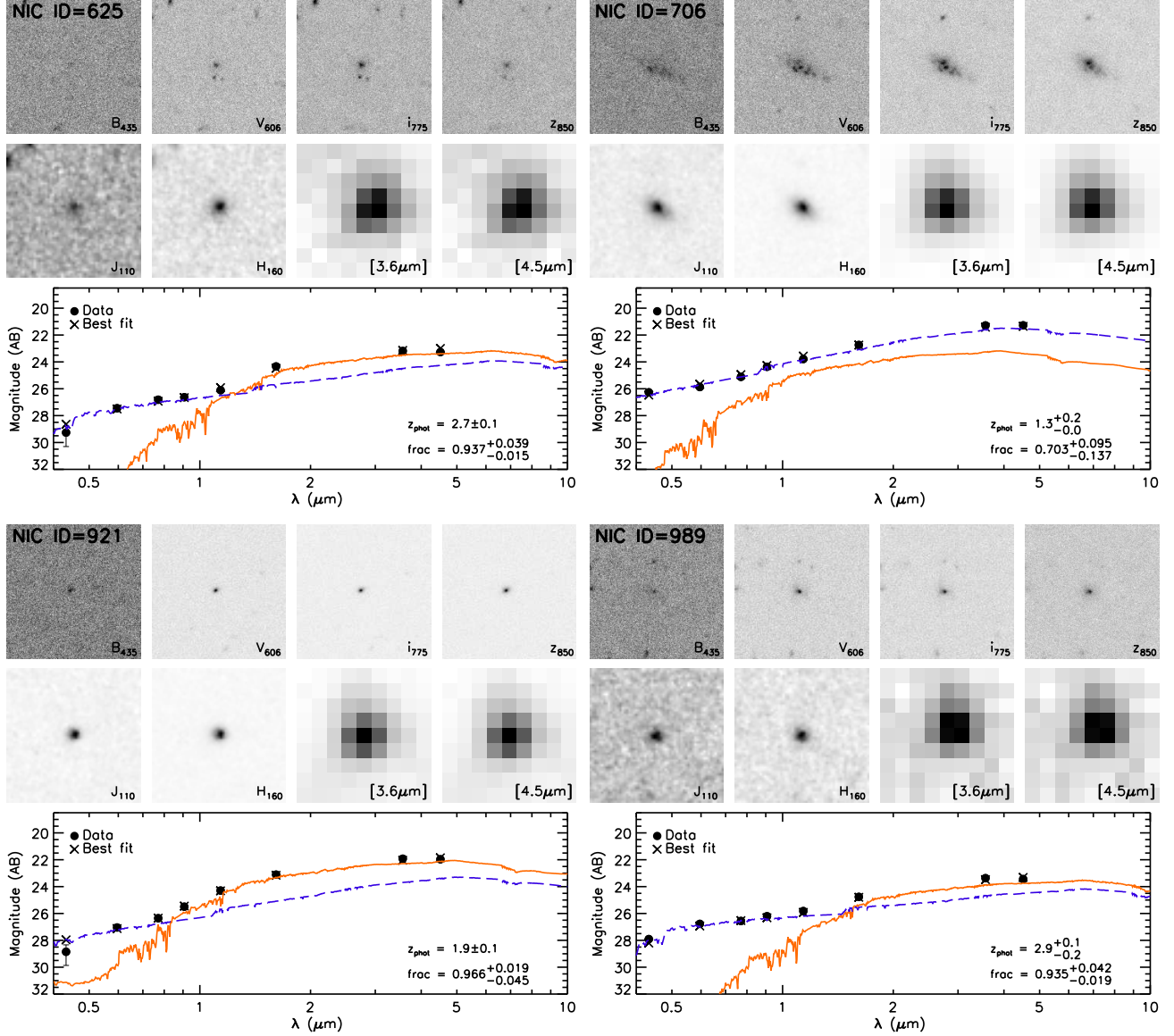


FIG. 7.— Same as figure 5.

for this object. This object is detected at $24\mu\text{m}$ with $f_{\nu}(24\mu\text{m}) = 110 \mu\text{Jy}$, supporting the interpretation that this object is a lower redshift dust-enshrouded starburst.

NIC ID = 625: The most-likely model is consistent with a distant galaxy dominated by mass by an old stellar population with a small amount of ongoing star formation ($z_{\text{phot}} = 2.7 \pm 0.1$ and $f_{\text{old}} = 0.94$). The redshift derived without the IRAC data is higher, although poorly constrained, $z_{\text{phot}} = 3.3 \pm 0.4$, and the stellar population remains dominated by an old population. Chen & Marzke (2004) derive a redshift for this object of $z_{\text{phot}} = 3.33$, consistent with our fit excluding the IRAC data (see table 2).

NIC ID = 706: The most-likely model is consistent with a low-redshift dusty star forming galaxy. Chen & Marzke (2004) reach a similar conclusion for this object.

NIC ID = 921: The fitting results are consistent with an intermediate redshift old stellar population, with $z_{\text{phot}} = 1.9 \pm 0.1$ and $f_{\text{old}} = 0.97$. Daddi et al. (2005) measure

a consistent result with a spectroscopic redshift of $z = 1.98$. Yan et al. (2004a) also derive a similar photometric redshift. Our mass, $8 \times 10^{10} M_{\odot}$ is in good agreement with the mass derived by Daddi et al. (2005).

NIC ID = 989: The resulting model fit is consistent with a distant galaxy dominated by mass by an old stellar population and with a small amount of ongoing star formation ($z_{\text{phot}} = 2.9$ and $f_{\text{old}} = 0.94$). Exclusion of the IRAC data yields a similar model.

NIC ID = 1078: The most-likely model parameters derived from the HST+IRAC data are consistent with a distant, $z_{\text{phot}} = 2.9^{+0.7}_{-0.3}$, young and dusty stellar population, with a fitted $f_{\text{old}} = 0.4$ and $E(B - V) = 1.0$, although the redshift is not particularly well constrained. Fitting the photometry while excluding the IRAC data gives a consistent redshift, but a very different interpretation of this object. In this case the model is dominated by an old stellar population, with $f_{\text{old}} = 1.0$. The relatively bright IRAC flux densities, taken in conjunction with

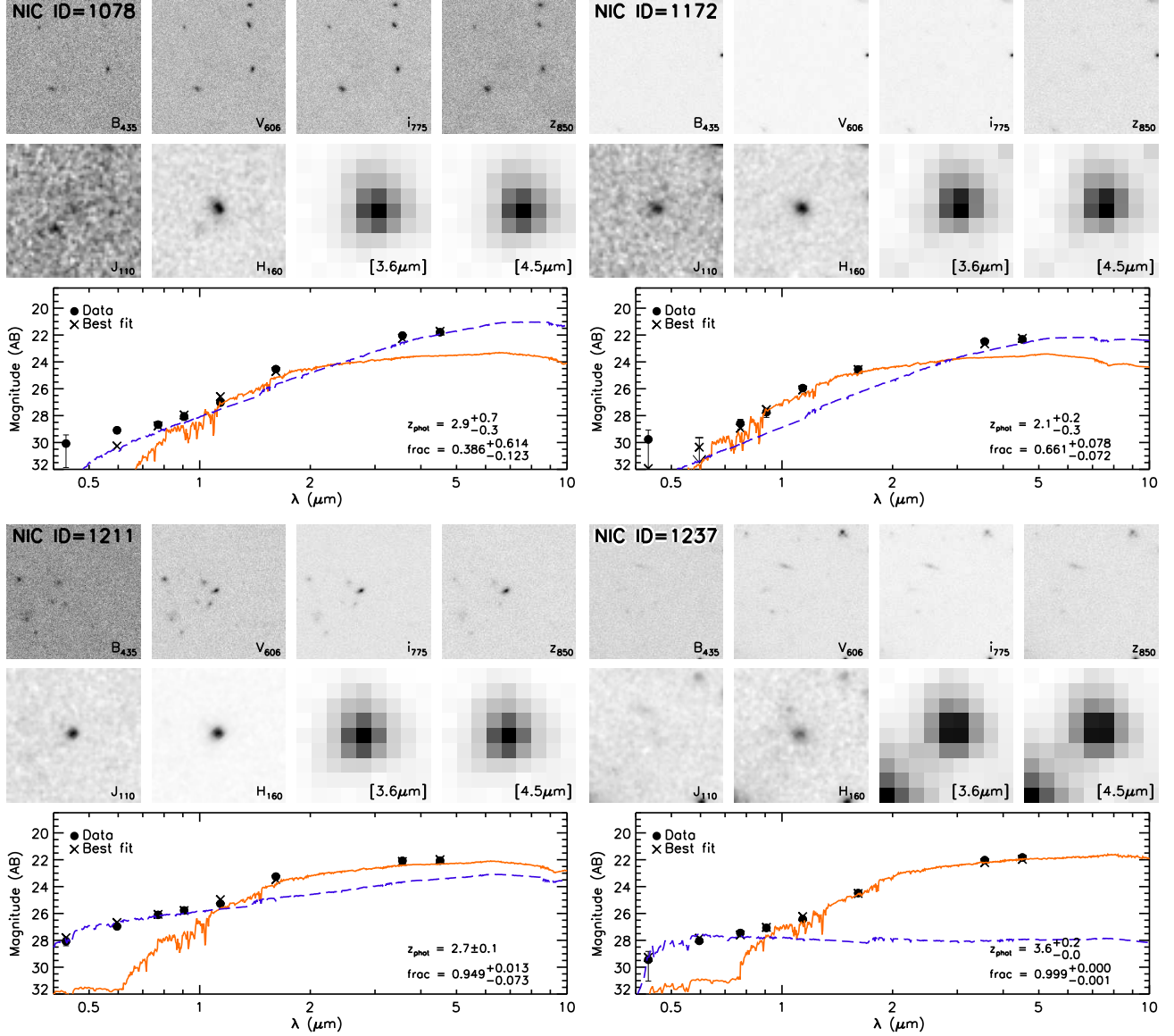


FIG. 8.— Same as figure 5, arrows indicate 1σ upper limits.

the HST photometry, are inconsistent with our models of old stellar populations, which require a flattening of the SED at wavelengths blueward of about $0.5\mu\text{m}$ rest-frame. Chen & Marzke (2004) derive a $z_{\text{phot}} = 2.91$, in good agreement with our results. However, they find that this object is consistent with a E/S0 SED, far more evolved than the constant star-forming model we derive when we include the IRAC data. Yan et al. (2004a) select this object using a $f_{\nu}(3.6\mu\text{m})/f_{\nu}(z_{850}) > 20$ selection and derive a $z_{\text{phot}} = 3.6$, also consistent with our poorly constrained z_{phot} . Yan et al. (2004a) do not include this object in their analysis due to the large uncertainties in their fitted redshift. However, we note that Yan et al. (2004a) report a non-detection for this object ($z_{850} > 29.5$ mag; using data from Yan & Windhorst 2004c), while we report a detection of $z_{850} = 28.1$ mag. Upon inspection of the unconvolved ACS z-band image, we see low surface brightness flux at the location of this object and we measure a detectable flux in our PSF-convolved im-

age. Incidentally, although the analysis of Mobasher et al. (2005) supports a very high redshift interpretation for this object ($z > 6$), subsequent analyses by Dunlop et al. (2007, MNRAS, 376, 1054) and Chary et al. (2007) favor an interpretation that this source resides at substantially lower redshift $z < 4$, consistent with our interpretation.

NIC ID = 1172: This object's most-likely model parameters are consistent with an intermediate redshift old stellar population with a significant amount of UV-bright younger stars: $z_{\text{phot}} = 2.1^{+0.2}_{-0.3}$ and $f_{\text{old}} = 0.66$. Yan et al. (2004a) derive a $z_{\text{phot}} = 2.7$, somewhat larger than our value of z_{phot} .

NIC ID = 1211: The resulting model fit is consistent with a distant galaxy whose mass is dominated by an old stellar population. We derive a $z_{\text{phot}} = 2.7 \pm 0.1$ and an $f_{\text{old}} = 0.95$. Chen & Marzke (2004), Daddi et al. (2005), Toft et al. (2005) and Yan et al. (2004a) derive $z_{\text{phot}} = 3.43, 2.47, 3.24, 2.8$ respectively. We suspect the discrepancies between the different fits result from as-

assumptions about the star-formation histories of the models and differences in the photometry. Our derived mass, $M_{tot} = 1.1 \times 10^{11} M_{\odot}$, is higher than, but not inconsistent with, the mass derived by Daddi et al. (2005). Although this object is selected by Chen & Marzke (2004) they do not report its mass as they classify it as a dusty starburst. This object has an upper limit X-ray flux of $f(0.5 - 2\text{keV}) = 3.7 \times 10^{-17} \text{ ergs cm}^{-2} \text{ s}^{-1}$ (Alexander et al. 2003), implying the possible presence of an AGN. However, the rest-frame UV through IR photometry is consistent with integrated stellar populations and therefore we include this object in our sample of distant, evolved galaxies.

NIC ID = 1237: This object's best-fit model is consistent with a distant, old stellar population: $z_{\text{phot}} = 3.6$ and $f_{\text{old}} = 0.999$. The exclusion if the IRAC data gives a similar fit, $z_{\text{phot}} = 3.3$ and $f_{\text{old}} = 0.998$. Chen & Marzke (2004) derive a much higher redshift for this object, $z_{\text{phot}} = 4.25$. Yan et al. (2004a) also select this object but do not consider it due to the fact that their $z_{\text{phot}} = 3.4$ is very uncertain. We note that our photometry for this object is likely biased because of the proximity of a very bright spiral galaxy, just visible in the lower left corner of fig. 8. It is likely that the image convolution causes low-surface-brightness emission for this objects to enter our aperture. Furthermore, our photometry could be biased by the presence of nearby, faint sources in the ACS data that might be blended with this source at the NICMOS H-band resolution. This object also has a marginal $24\mu\text{m}$ detection due to the fact that it is blended, with $f_{\nu}(24\mu\text{m}) = 76 \mu\text{Jy}$, which may call in to question the validity of the best-fit model. Because of these reasons we reject this object as a candidate for a distant, evolved galaxy.

We note that although our photometry is generally in good agreement with other published values which we are aware of, a few of our objects have significant differences (notably NIC ID 1078 and 1237). In the case of NIC ID 1078, we suspect our photometry is appropriate for our NICMOS-selected catalog. For NIC 1237, scattered light from a nearby, large galaxy likely affects our photometry measurements. Regardless, neither of these objects enters our final sample for galaxies whose mass is dominated by older stellar populations, so these do not affect our final conclusions.

We derive masses assuming a Salpeter IMF, where the Bruzual & Charlot (2003) models use upper and lower mass cutoffs of $100 M_{\odot}$ and $0.1 M_{\odot}$. For an SSP Bruzual & Charlot (2003) model, assuming a Chabrier IMF would decrease our masses by a factor of 1.8, relative a Salpeter IMF and for the same assumed upper and lower mass cutoffs listed above. For a more detailed discussion of how masses depend on the IMF parameters such as the slope and the mass cutoffs, see Papovich et al. (2001). We note that Chen & Marzke (2004) identify red objects in the HUDF and derive masses for six early-type candidates, 4 of which are systematically lower than the masses derived here. Our overlap objects are 219, 223, 625, 1078, and 1237. The total H-band magnitudes also differ for these objects; as expected, there is a rough trend between increasing flux discrepancy and increasing mass discrepancies. Object 223 has the largest difference in mass, a factor of ~ 40 . Objects 219, 625 and 1078 have masses that differ by factors of 18.0, 2.1 and 1.4, respec-

tively, from the Chen & Marzke (2004) masses, although the two estimates for objects 625 and 1078 are entirely consistent. Object 1237 is the only for which our mass is lower than the Chen & Marzke (2004) mass, by a factor of ~ 1.2 , but as stated previously, this likely results from the higher redshift derived by Chen & Marzke.

3.3. Other models

To investigate possible systematic dependences due to our modeling, we explore the effects of changing our model assumptions.

We first consider a single component fit using the same young model described above, a constant star forming model attenuated with the Calzetti et al. (2000) law. This model does not characterize our objects well, yielding very large χ^2 values compared to the two-component base model, with an average increase in $\chi^2 \sim 55$.

We also test a more complex dust model, the Witt & Gordon (2000) SMC shell geometry dust model. We try both a single component and a two-component fit with this dust model. The single component fit, a 100 Myr old constant star forming model with dust as a free parameter, does not characterize the data well; the best-fit χ^2 values are very large compared to our base model and to the single component fit using Calzetti et al. (2000) dust discussed above. The two component fit, the second component being a maximally old SSP model, results in an average χ^2 difference of $\langle \chi_{\text{best, base model}}^2 - \chi_{\text{best}}^2 \rangle = -1.5$ over all 16 objects, somewhat worse than our base model. This dust model gives lower χ_{best}^2 values for 9 objects. Object 921 has the largest $\Delta\chi^2$ of 3.3. This dust model assigns systematically higher $E(B - V)$ values, in particular to objects 30, 625, 921 and 1211, with best-fit $E(B - V) = 1.4, 2.5, 5.3$ and 2.8 respectively. For completeness we note that the dust grid over which our models span is the grid provided by the Witt & Gordon (2000) look-up tables for this dust law. It is not the same grid as that in our base model and it is not a regularly varying grid, having values of $E(B - V)$ ranging from 0.0 to 12.3, in steps of $\Delta E(B - V) = 0.0875$ at low values and in steps of $\Delta E(B - V) = 1.75$ at high values. This difference may hamper our ability to make a fair comparison with our base model. However, we do not think this is the case as none of our original model fits have large values of $E(B - V)$, all objects having model fit values of $E(B - V) \leq 1.1$. We note that the best-fit masses differ by less than a factor of 3.6 between this model and our base model, excluding object 319, whose mass increases by about an order of magnitude relative to our base model. Similarly, the fractions change by small amounts: $\langle |\Delta f_{\text{old}}| \rangle = 0.08$ over the set of 16 objects. The only objects with a significant change in redshift are 88, 319 and 1172 with a $\Delta z_{\text{phot}} = 0.9, 1.1$ and 1.1 respectively. None of these objects are included in our final sample of galaxies whose mass is dominated by older stellar populations.

We next consider the possibility that our objects have metallicities lower than solar. Again, we perform a similar analysis as outlined above, with both the young and old models at the same ages as for our base model and using the Calzetti et al. (2000) dust law, but with both components at a metallicity of $0.2Z_{\odot}$. For this model,

TABLE 4
COMPARISON BETWEEN TABLE 3 AND THE τ -MODEL FITTING

NIC ID	z_{phot}	z_{phot}^{τ}	$\log M_{\text{TOT}}/M_{\odot}$	$\log M_{\text{TOT}}/M_{\odot}^{\tau}$	f_{old}	Age (Gyr) $^{\tau}$	τ (Gyr)	$\chi^2_{\nu, \text{best}}$	$\chi^2_{\nu, \text{best}}^{\tau}$
30	1.8	1.5 ± 0.1	11.5	11.2 ± 0.1	0.984	1.47 ± 0.36	$1.19^{+0.71}_{-0.32}$	9.2	8.4
88	2.2	$2.0^{+0.2}_{-0.5}$	10.9	$10.8^{+0.1}_{-0.3}$	0.718	$0.08^{+0.24}_{-0.02}$	$0.01^{+0.74}_{-0.01}$	0.7	1.3
111	1.5	0.8 ± 0.1	9.6	$7.8^{+0.0}_{-0.2}$	0.914	0.14 ± 0.11	0.13 ± 0.10	11.3	4.5
120	3.4	2.3 ± 0.2	11.1	$10.5^{+0.3}_{-0.4}$	0.994	$0.39^{+0.92}_{-0.36}$	$0.91^{+9.92}_{-0.90}$	2.0	1.2
219★	2.8	2.5 ± 0.1	11.1	10.9 ± 0.1	0.982	$0.80^{+0.14}_{-0.29}$	0.36 ± 0.16	2.2	2.0
223★	3.1	$2.3^{+0.7}_{-0.1}$	11.4	11.1 ± 0.1	0.995	$0.86^{+0.44}_{-0.19}$	$0.81^{+3.09}_{-0.63}$	0.7	1.0
269★	2.7	2.6 ± 0.1	10.4	10.1 ± 0.1	0.944	$0.75^{+0.19}_{-0.22}$	$1.68^{+11.0}_{-1.13}$	1.9	2.2
319	1.2	$1.0^{+0.0}_{-0.1}$	10.5	$10.4^{+0.1}_{-0.2}$	0.344	$0.08^{+0.09}_{-0.06}$	$0.25^{+3.84}_{-0.25}$	1.3	0.9
625★	2.7	2.7 ± 0.1	10.6	10.3 ± 0.1	0.937	$0.19^{+0.23}_{-0.08}$	$0.04^{+0.06}_{-0.03}$	3.3	1.1
706	1.3	1.2 ± 0.1	10.4	10.2 ± 0.3	0.703	$0.13^{+0.60}_{-0.09}$	$0.71^{+7.17}_{-0.08}$	4.2	2.8
921	1.9	$1.9^{+0.2}_{-1.4}$	10.9	$10.6^{+0.1}_{-1.8}$	0.966	$0.26^{+0.1}_{-0.23}$	$0.01^{+0.69}_{-0.01}$	1.6	1.6
989★	2.9	2.5 ± 0.2	10.5	$10.1^{+0.1}_{-0.3}$	0.935	$0.47^{+0.34}_{-0.37}$	$0.68^{+4.35}_{-0.61}$	1.3	2.2
1078	2.9	$2.7^{+0.2}_{-0.1}$	11.0	11.2 ± 0.1	0.386	$0.53^{+0.75}_{-0.40}$	$0.12^{+0.18}_{-0.11}$	5.8	1.2
1172	2.1	$1.4^{+0.3}_{-0.5}$	10.6	$10.4^{+0.2}_{-0.4}$	0.661	$0.52^{+0.56}_{-0.41}$	$0.01^{+0.11}_{-0.01}$	1.0	0.5
1211★	2.7	2.8 ± 0.1	11.1	10.9 ± 0.1	0.949	0.34 ± 0.11	0.09 ± 0.01	5.0	1.7
1237	3.6	$2.7^{+0.2}_{-0.1}$	11.2	$11.2^{+0.1}_{-0.2}$	0.999	$1.03^{+0.66}_{-0.41}$	$0.72^{+0.54}_{-0.45}$	1.9	0.5

NOTE. — The columns with τ -model parameters are indicated with a τ symbol. The six galaxies with broad-band SEDs consistent with distant evolved stellar populations are marked with a star symbol.

the average difference in χ^2 is $\langle \chi^2_{\text{best, base model}} - \chi^2_{\text{best}} \rangle = -2.1$, i.e., our base model does a better job at fitting our object SEDs. This set of low-metallicity models yields a lower χ^2_{best} for four of our objects. For the entire set of 16 objects the change in redshift is $\langle |\Delta z_{\text{phot}}| \rangle = 0.3$, with object 30 having by far the largest difference: $z_{\text{phot, base model}} - z_{\text{phot}} = -1.3$. The best-fit masses change little, with a variation smaller than a factor of ~ 3 for all objects. The stellar populations remain consistent for all 16 objects except 1237, which is fitted as a young starburst with $f_{\text{old}} = 0.07$, as opposed to our base model fit with $f_{\text{old, base model}} = 0.999$. This result lends credence to the interpretation supported by the $24\mu\text{m}$ and X-ray data that this object may host an obscured AGN. We note that altering the metallicity of the base model does not significantly change the fitting results for the 6 objects we select as candidates for distant, evolved galaxy candidates and therefore will not affect our final conclusions.

We also consider the effects of a dusty old population; we fit our data using the two-component base model outlined above and we use Calzetti et al. (2000) dust to attenuate the old component with $E(B-V) = 0.05$ (or an $A_V = 0.2$). For this model we calculate an average χ^2 change of $\langle \chi^2_{\text{best, base model}} - \chi^2_{\text{best}} \rangle = 4.1$. We derive χ^2_{best} that are lower than those derived with our base models for 11 objects (NIC ID = 30, 88, 111, 120, 269, 625, 706, 986, 1078, 1172, and 1211). For this sub-set, objects 111, 625, 1078, and 1211 have the largest differences, with $\Delta\chi^2 = 32.9, 9.0, 11.7$, and 6.2 respectively. The other 7 objects all have $\Delta\chi^2 < 3.3$. The photometric redshifts change little, with a $\langle |\Delta z_{\text{phot}}| \rangle = 0.15$ for all objects, except 111, which has a $\Delta z_{\text{phot}} = 1.9$. The mass fractions in old and young stars change little, with $\langle |\Delta f_{\text{old}}| \rangle = 0.03$ for all objects except 219 and 1237, both of which have a decrease in f_{old} of $f_{\text{old, base model}} - f_{\text{old}} = 0.9$. For the 6 objects we consider distant, evolved galaxy candidates, the derived masses change by less than 50%.

Finally, we consider single-component τ -models with

varying ages similar to other studies in the literature. We summarize the fitting results here and compare, in more detail, the best-fit τ -model parameters with our base model results in Table 4. We generate models over a grid in ages and τ values, where τ is the exponential timescale for decay in star-formation. Our age grid values are 0.01, 0.02, 0.04, 0.06, 0.08, 0.10, 0.20, 0.50, 0.70, 1.00, and 2.00 Gyr, and our τ grid spans 0.001 Gyr to 20.0 Gyr in quasi-logarithmic steps. We use the same redshift and dust grid as that of our base model and we assume the same dust attenuation law, the Calzetti et al. (2000) law. We fit the observed SEDs of our selected objects using this 4-dimensional grid of models. With these models we obtain lower χ^2_{best} values, relative to our base model, for 11 objects (NIC ID = 30, 111, 120, 219, 319, 625, 706, 1078, 1172, 1211, and 1237), with objects 111, 1078, and 1211 having the largest differences of $\Delta\chi^2 = 27, 18$, and 13 , respectively. For all 16 objects we measure a change in χ^2 of $\langle \chi^2_{\text{best, base model}} - \chi^2_{\text{best}} \rangle = 5.0$; if we exclude objects 111, 1078, and 1211, the change in χ^2 becomes $\langle \chi^2_{\text{best, base model}} - \chi^2_{\text{best}} \rangle = 1.7$. The masses of the 11 objects with lower $\chi^2_{\text{best, } \tau}$ change by less than a factor 2 with respect to the base model fit, the only exceptions being objects 111 and 120, which have factors of ~ 60 and ~ 3 decrease in mass respectively. The fitted redshifts do not change significantly, $\langle z_{\text{phot, base model}} - z_{\text{phot}} \rangle = 0.3$, with objects 111, 120, and 1172 having the largest change of $\Delta z_{\text{phot}} \sim 0.7, 1.0$, and 0.7 respectively. For the entire sample of 16 it is interesting to note that 14/16 objects have base model masses that are higher than those derived with the τ -models. We consider this to be a consequence of the fact that our base model is better suited to measure an upper limit on the masses of our objects; this is in part because the maximally old component of this model has a limiting mass to light ratio. Furthermore, we note that for the 6 objects with distant evolved fits, we derive masses which are between a factor of 1.3 and 2.5 greater than those derived from the τ -model fits. Therefore we conclude that our adopted two-component

base model is better suited to place upper limits on the old stellar population census in our objects than the τ -model. We note that the two objects with higher τ -model masses are 1078 and 1237, which are greater by a factor of 1.6 and 1.1, respectively, still consistent within the errors with our base model.

We conclude that a two-component fit is better able to characterize the data than a one-component fit and that, although some objects are better fit by other models, in general our base model characterizes our objects well. We show that the changes in our fitted redshifts, total masses and fractions (f_{old}) are not strongly dependent on the assumed metallicity and dust properties of our models.

4. DISCUSSION AND SUMMARY

We have investigated the physical properties of 32 galaxies selected with $(J_{110} - H_{160}) > 1.0$ colors in the HUDF using deep, broadband imaging from *HST* and *Spitzer*. Exactly half of these objects (16/32) have unblended IRAC $[3.6\mu\text{m}]$ and $[4.5\mu\text{m}]$ photometry. Here, we focus on the subset of galaxies with IRAC photometry because the data span a longer wavelength baseline, allowing us to separate more cleanly the objects into those whose colors are consistent with dust-enshrouded starbursts and those dominated by old stars. Thus, where we derive number densities and mass densities, we include a factor of 2 correction for incompleteness due to blending in the IRAC image. Furthermore, including both the *Spitzer*/IRAC data allows us to better constrain the properties of the galaxies' stellar populations (see further discussion in, e.g., Labbé et al. 2005; Papovich et al. 2006).

4.1. The Properties of Galaxies with Evolved Stellar Populations at $z \gtrsim 2.5$

Based on the full SED fitting, we split the subsample of objects with IRAC photometry into two broad categories: those objects whose broad-band SEDs are well represented by our two component model with a substantial component of evolved stars combined with a young star-forming component, and those objects whose interpretation changes substantially by including the IRAC photometry compared to the model fits to only the ACS and NICMOS data. For 12/16 (75%) of the objects, including the IRAC data give roughly consistent best-fit models as to the ACS and NICMOS data only (NIC IDs 88, 219, 223, 269, 319, 625, 706, 921, 989, 1172, 1211, and 1237). Because we are primarily interested in placing constraints on the number density of galaxies dominated by passively evolving stellar populations, we focus here on the subset of galaxies whose model fits have $z \geq 2.5$ and $f_{\text{old}} \geq 0.9$. That is, the models favor a scenario where the vast majority of the galaxy's stellar mass resides in an older, passively evolving component. There are 6 objects satisfying these conditions (NIC IDs 219, 223, 269, 625, 989, and 1211).

For three of these objects (NIC IDs 223, 625, 989), we have higher-confidence redshifts due to the presence of a Lyman "break" between in the $B_{435} - V_{606}$ colors. This occurs for galaxies with relatively blue rest-frame UV colors, and a characteristic "break" in the colors as neutral hydrogen attenuation from the IGM absorbs the intrinsic flux shortward of 1216 \AA (e.g., Madau 1995). For the

ACS filters, absorption owing to IGM neutral hydrogen affects the B_{435} -band at $z \gtrsim 3$, and the presence of this break drives the estimate of the redshifts for these galaxies ($z_{\text{phot}} \simeq 3.5, 3.2$, and 3.1 , respectively). Interestingly, at $z \sim 3 - 3.5$ the Balmer/4000 \AA is moving through the H_{160} -band, diminishing the $J - H$ color. Therefore the fact that these galaxies have $J_{110} - H_{160} \geq 1$ mag implies they need a relatively large fraction of their stellar mass in older populations, and in all cases we find best fits with $f_{\text{old}} > 0.93$.

Chen & Marzke (2004) used a NICMOS-selected catalog in the HUDF combined with photometric redshifts to select six candidates for massive, red ($i_{775} - H_{160} \geq 2$) early-type galaxies at $z > 3$. Interestingly, for only 2 of their candidates where we have IRAC data does our analysis reach the conclusion that old stellar populations dominate the observed colors (NIC IDs 223, 625). We find for three of their candidates (NIC IDs 219, 1078, 1237) that when the IRAC data are included the SED fits favor solutions where most of the light originates from dusty, young stellar populations. For the remaining candidate of Chen & Marzke, we do not have IRAC data but our SED fit to the existing ACS + NICMOS photometry does favor a solution where the galaxy is dominated by older stellar populations.

For three of our six objects with IRAC photometry, $z \geq 2.7$, and $f_{\text{old}} \geq 0.9$ (NIC IDs 269, 989, and 1211), Chen & Marzke (2004) do not include these in their sample of evolved galaxies. We derive a photometric redshift, $z = 2.7$, for NIC ID 269, slightly below the $z > 2.8$ selection of Chen & Marzke, which may be the reason they excluded it. Chen & Marzke interpret object NIC ID 1211 to be dominated by a dusty starburst. However, the H_{160} to $[3.6\mu\text{m}]$ and $[4.5\mu\text{m}]$ colors imply that while its rest-frame UV light stems from dust-obscured young stars, most of the mass ($>88\%$ at 68% confidence) resides in evolved stellar populations (see figure 8; however, we note that the upper limit on the X-ray detection of this galaxy may imply that it hosts an AGN, see § 3.2). NIC ID 989 appears to have some ongoing star formation (with relatively blue B_{435} to z_{850} colors), but older stars appear to dominate the rest-frame optical and near-IR light (figure 7). We suspect this object was excluded from the selection of Chen & Marzke because of its relatively blue ACS colors. Regardless, we find that data at wavelengths greater than rest-frame $1 \mu\text{m}$ are required for interpreting the properties of the stellar populations of red galaxies.

Parenthetically, we note that there are two objects in the HUDF with $J_{110} - H_{160} > 2$ mag (NIC IDs 1078, 1211) and one object has $J_{110} - H_{160} = 1.95$ mag (NIC ID 1237). All three have IRAC photometry. These objects have colors comparable to the "unusual" red, $J_{110} - H_{160}$ -selected object in the HDF-N reported by Dickinson et al. (2000), which has $J_{110} - H_{160} \simeq 2.3$ mag. Based on our fits to the ACS, NICMOS, and IRAC photometry of the HUDF objects, we conclude that two (NIC IDs 1078, 1237) are dominated by dusty starbursts, while only one (NIC ID 1211) is dominated by a substantial population of old stars. Dickinson et al. (2000) are unable to distinguish between these two possibilities (or, for that matter, the possibility that their object is a $z \approx 12$ Lyman-break-type galaxy). This is partly because the HDF-

N object is undetected in the *HST*/WFPC2 data, nor did it have longer wavelength data from *Spitzer*/IRAC. Two of the three objects here have *HST*/ACS photometry $\gtrsim 1$ mag fainter than the detection limit of the WFPC2 data in the HDF-N. Therefore, we conclude that one requires *very* deep *HST* optical imaging and *Spitzer*/IRAC imaging to constrain the nature of these very red, $J_{110} - H_{160} \gtrsim 2$ mag objects.

None of our six candidates for galaxies with substantial population of evolved stellar stars is entirely devoid of recent star formation (i.e., all objects have $f_{\text{old}} < 1.0$). Indeed, in the entire HUDF there are *no* candidates for galaxies consistent with a purely passively-evolving stellar population formed at much higher redshift (and in the NICMOS HDF-N, there is only one possible candidate, see discussion above; Dickinson et al. 2000). Therefore, such objects are extremely rare if they exist at this redshift. We conclude that at $z \gtrsim 2.5$ even galaxies with a substantial amount of evolved stellar populations still maintain some ongoing star-formation. Papovich et al. (2005) argue based on galaxies' morphologies that at $z \gtrsim 2$, recurrent star-formation dominates the rest-frame UV and blue light, which will maintain some level of homogeneity in the galaxies' internal colors. Our interpretation here is consistent with that scenario. However, we note that it appears that while the young stellar populations dominate the UV and blue light, in a small fraction of galaxies a substantial population of older stars dominates at rest-frame wavelengths $\gtrsim 1 \mu\text{m}$.

4.2. Galaxies with Evolved Stellar Populations at $z > 1.5$

With the $J_{110} - H_{160} > 1$ mag selection, we identify massive galaxies with substantial stellar mass and with SEDs dominated by the light from passively evolving stellar populations. Figure 9 shows the measured H_{160} magnitudes as a function of redshift for galaxies with $f_{\text{old}} > 0.9$, for objects with IRAC photometry (right panel) and without IRAC photometry (left panel). Although the data should be sensitive to such objects down to our selection limit, $H_{160} < 26$ mag, only one such object has $25 < H_{160} < 26$ mag — the rest have $H_{160} < 25$ mag. Figure 10 shows the derived stellar masses as a function of galaxy redshift for all galaxies in the $J_{110} - H_{160} > 1$ mag sample. The figure shows the stellar masses derived for the whole sample using only the ACS through NICMOS data (left panel), and it shows the stellar masses derived including the IRAC data for the IRAC-detected subsample (right panel). Objects with more than 90% of their stellar mass in evolved stellar populations are circled in the figure. There exist objects whose light (and stellar mass) is dominated by passively evolving stellar populations with total stellar masses up to and exceeding $>10^{11} M_{\odot}$ over the entire redshift range. The existence of these galaxies is not entirely unexpected, given that such objects likely dominate the stellar mass density even at $z \sim 2$ (e.g., Rudnick et al. 2006; van Dokkum et al. 2006).

However, there is an apparent dearth of objects whose light is dominated by passively evolving stellar populations with lower stellar masses. For example, none of the 10 IRAC-detected galaxies with $z_{\text{phot}} > 1.6$ and with more than 90% of their stellar masses evolved stellar populations are fainter than $H_{160} > 25$ mag (see

figure 9), which is one magnitude above our detection limit. (We note there is one object with $z_{\text{phot}} \simeq 1.5$ and $H = 25.5$ mag, and a derived total stellar mass $4 \times 10^9 M_{\odot}$, see figure 9.) Therefore, at these high redshifts, the candidates for passively evolving galaxies are already massive. In terms of total stellar mass, the right-hand panel of figure 10 shows that all the IRAC-detected objects with $f_{\text{old}} > 0.9$ and $z > 1.5$ have stellar masses greater than $\sim 2 \times 10^{10} M_{\odot}$. If we instead consider the results for galaxies from their stellar masses derived without the IRAC data, there is only a single candidate as a low-mass galaxy whose mass is dominated by passively evolved stellar populations (and we consider the stellar masses derived in the old component without IRAC data to be less robust).

The data should be sensitive to objects dominated by old stellar populations with stellar masses with $\sim 3 \times 10^9$ to $10^{10} M_{\odot}$ (see figure 4 and figure 10). We note that this is not a bias related to the sources with IRAC detections. The IRAC data from GOODS ($5.8 \mu\text{m}$ flux density of $0.11 \mu\text{Jy}$, 5σ) would detect a passively evolving stellar population formed at $z=7$ and $M > 10^{9.5} M_{\odot}$ for all redshifts considered here.

Any plausible mass function for galaxies at $z \sim 2$ would predict a greater number of galaxies with lower stellar masses than at high stellar mass. For example, using the Fontana et al. (2006) empirical galaxy mass function, we would expect roughly double the number of galaxies with $0.5 - 2.0 \times 10^{10} M_{\odot}$ compared to those with $>2 \times 10^{10} M_{\odot}$. This strongly contrasts with the findings here for the red galaxies dominated by passively evolving stellar populations. Therefore, the data suggest that galaxies with more than 90% of their stellar mass in evolved stellar populations have a minimum mass threshold of roughly several times $10^{10} M_{\odot}$ at $z \sim 2$. The lack of such objects with lower masses may be related to the processes governing stellar mass build-up in galaxies at these redshifts.

4.3. Constraints on the Densities of Galaxies with Evolved Stellar Populations at $2.5 < z < 3.5$

With the full multiwavelength dataset, we have separated our sample into those galaxies that are dominated by dust-enshrouded starbursts and those galaxies whose rest-frame optical and near-IR emission is consistent with being dominated by a substantial population of evolved stars (see, e.g., section 4.2, above). Of the 16 $J_{110} - H_{160} > 1$ mag galaxies with robust IRAC photometry, 6 have best-fit models favoring a substantial population of evolved stellar populations, which is 37.5% of the sample. Extending this to the full sample of 32 galaxies with $J_{110} - H_{160} > 1$ mag, we estimate there should be 12 such objects in the area of the HUDF. Using these numbers, we place constraints on the number and mass density for these types of objects. If some of our 6 candidates for evolved stellar populations turned out to be dusty starbursts, our numbers would be reduced. Due to the lower mass to light ratios of younger models, the fitted masses would also be reduced. Therefore the densities derived here should be regarded as upper limits.

The HUDF data reach very deep limits in stellar mass for galaxies dominated by evolving stellar populations. For a galaxy whose stellar mass formed *in situ* at $z_f = 7$, the $H_{160} = 26.0$ mag detection limit corresponds to a

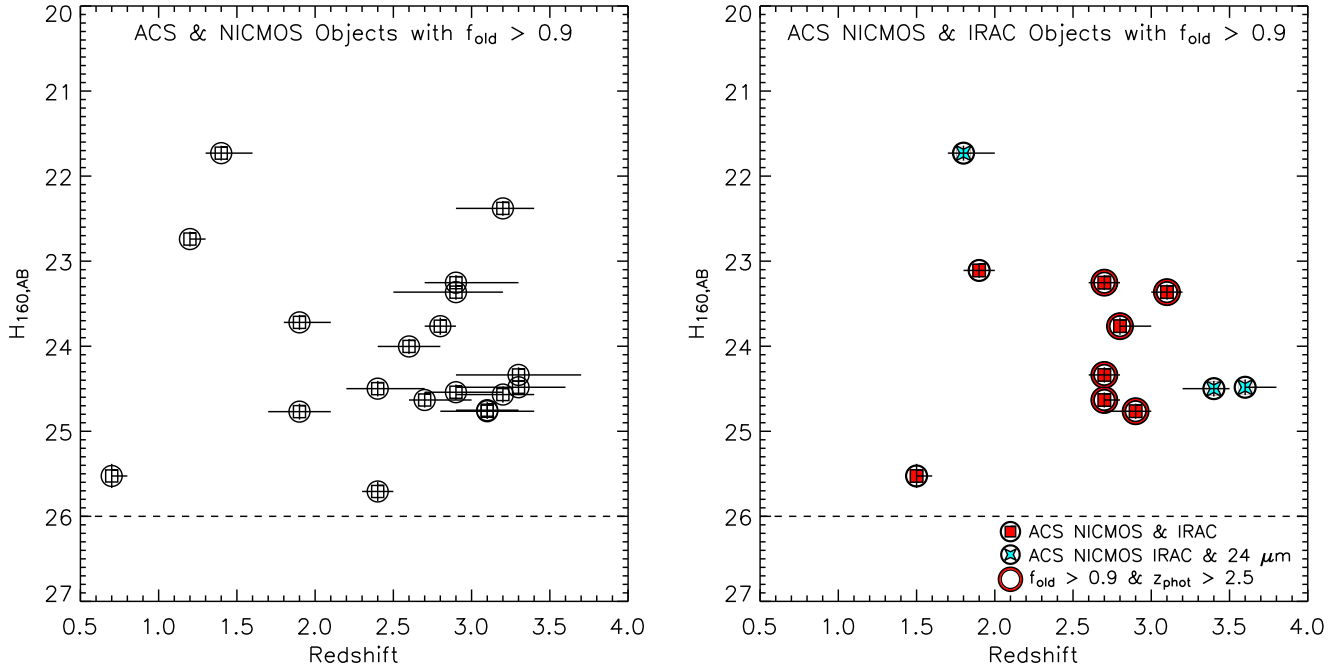


FIG. 9.— $H_{160,AB}$ magnitudes vs. photometric redshifts for the subset of $(J_{110} - H_{160})_{AB} > 1.0$ mag objects with best-fit $f_{old} > 0.9$, for objects without IRAC photometry (left panel) and with IRAC photometry (right panel). The dashed line shows the $H_{160,AB} < 26$ magnitude cut. In the right-hand panel, cyan stars indicate those sources among the IRAC-detected subsample with $f_{old} > 0.9$ which have $24 \mu\text{m}$ detections. Thick-circles denote objects with $f_{old} > 0.9$ and $z_{phot} > 2.5$.

limit in stellar mass ranging from $6 \times 10^9 M_{\odot}$ at $z = 2$ to $1 \times 10^{11} M_{\odot}$ at $z = 4$ (see figures 4 and 10). Although the $(J_{110} - H_{160}) > 1$ mag color selection should be, in principle, sensitive to old stellar populations at $z \gtrsim 2$, in practice we find candidates for galaxies dominated by passively evolving stellar populations $f_{old} > 0.94$ at $z \geq 2.7$. Likewise, at $z > 3.5$, the Balmer/4000Å-breaks move beyond the F160W bandpass, making our color selection less efficient. Therefore, to set an upper limit on the number and mass densities of galaxies dominated by passively evolving stellar populations, we limit our redshift range to $2.5 < z < 3.5$. We note that requiring an IRAC detection does not limit our stellar mass selection; the limiting stellar mass for the IRAC GOODS data sensitivity limit is always less than that for the NICMOS limit at these redshifts (see above).

The volume in the area of the HUDF is $1.9 \times 10^4 \text{ Mpc}^3$ between $2.5 < z < 3.5$. Restricting our analysis to only those galaxies with $2.5 < z < 3.5$ we derive a number density of $3.1 \times 10^{-4} \text{ Mpc}^{-3}$, or $6.3 \times 10^{-4} \text{ Mpc}^{-3}$ including our 50% incompleteness. However, these six objects are not visible over the whole redshift range. In the number density calculation, we compute the effective volume, V_{eff} for each galaxy from $z = 2.5$ to z_{eff} , where z_{eff} is the lesser of $z = 3.5$ and the maximum redshift to which the galaxy could be detected. The number density derived by summing $\sum_i 1/V_{eff}^{(i)}$ over all i galaxies gives $3.3^{+1.0}_{-1.5} \times 10^{-4} \text{ Mpc}^{-3}$, and after accounting for incompleteness, $n = 6.6^{+2.0}_{-3.0} \times 10^{-4} \text{ Mpc}^{-3}$.

Assuming these objects will evolve to become present-day, passively evolving red galaxies, then this number density is significantly lower than what we would expect using local mass functions. Using the $z \sim 0$ mass func-

tion parameters listed in table 4 of Bell et al. (2003), we expect the number density of red, early-type galaxies to be $n(z=0) = 3.5 \times 10^{-3} \text{ Mpc}^{-3}$ in the volume spanned between $2.5 < z < 3.5$ in the HUDF (and again taking the redshift-dependent mass limit from figure 4)⁶. This is larger than the observed number density (including incompleteness) by roughly a factor of 5. Therefore, while we would have expected 65 objects in the HUDF (i.e., 32 after our 50% completeness) we have found only 6.

This difference is substantially larger than the Poisson noise ($\pm\sqrt{6}/6$, i.e., 40%). It may be that these objects suffer strong field-to-field clustering (possibly expected for red galaxies, e.g., Daddi et al. 2003; Quadri et al. 2007). We estimate the number error from density variations in the volume between $2.5 < z < 3.5$ in the HUDF as $0.3 \times \sigma_8$. While we have no measurement for σ_8 for these galaxies, based on theoretical models we expect $\sigma_8 \sim 1.0$ (Adelberger et al. 2005), implying that the error from density variations is 30%. Summing these errors in quadrature brings our total error estimate to $\approx 50\%$ for the expected number of these galaxies in the HUDF. Even so, the difference between the 32 expected galaxies and the 6 we find is substantially larger than the combined errors from counting statistics and cosmic variance. Therefore, by number, and recalling that these candidates only define upper limits, the objects in the

⁶ Note that (Bell et al. 2003) assumed a formation redshift, $z_f = 4$, in their mass functions. This is only marginally lower than $z_f = 7$ used in this analysis. However, the change in lookback time from $z \approx 0$ to 4 relative to that from $z \approx 0$ to 7 corresponds to a change in the mass-to-light ratio of $M/L_B = 5.8$ to 6.2. Applying our higher formation redshift to Bell et al. would increase their stellar masses by $\approx 5\%$, which is negligible compared to other uncertainties.

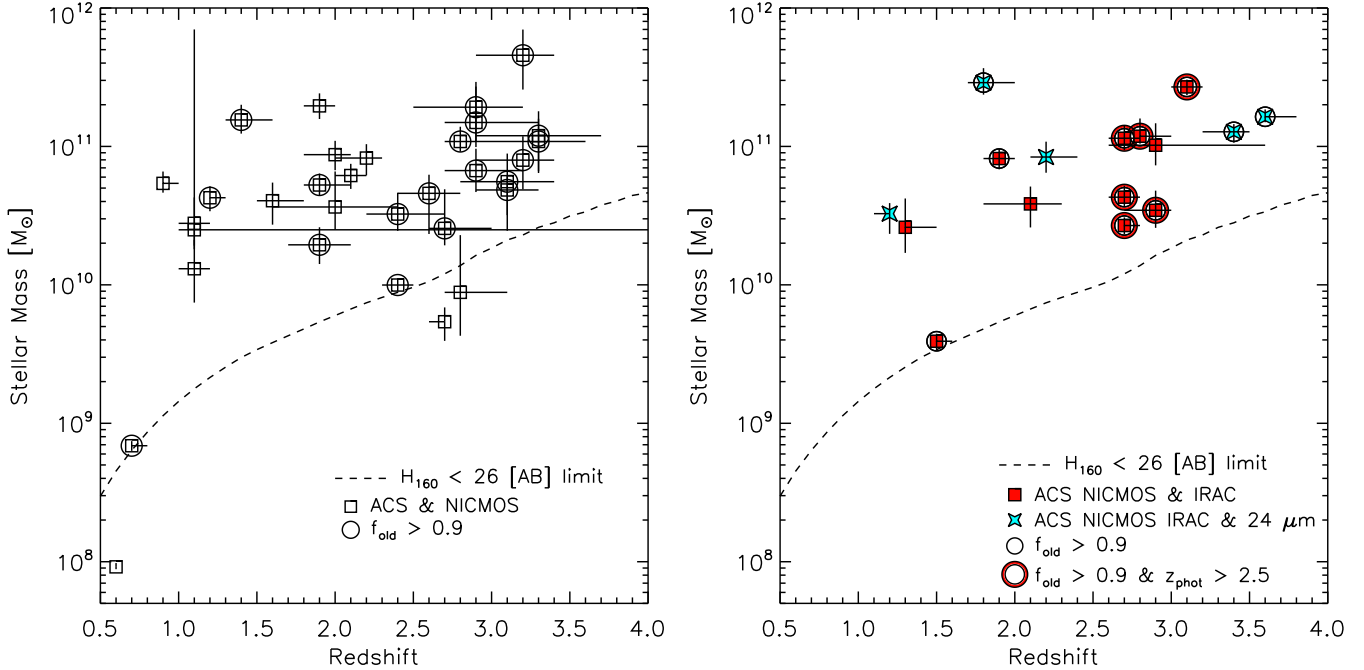


FIG. 10.— Best-fit model masses and photometric redshifts for all HUDF objects with $(J_{110} - H_{160})_{AB} > 1.0$ mag (left panel) and the subset of these with unblended IRAC photometry (right panel). The dashed line shows the limiting stellar mass for galaxies with a stellar population formed in a burst at $z = 7$ with observed magnitude $H_{160} = 26.0$. In both panels the open circles indicate objects dominated by old stellar populations ($f_{old} > 0.9$). In the right-hand panel, cyan stars indicate those sources among the IRAC-detected subsample with $24\ \mu\text{m}$ detections. Thick-circles denote those objects with $f_{old} > 0.9$ and $z_{phot} > 2.5$, which are the discussion of § 4.3.

HUDF which are dominated by evolved stellar populations make up less than one-third of present-day red, early-type galaxies. Thus, at least two-thirds of present-day red, early-type galaxies must assemble and/or evolve into their current configuration at $z \lesssim 2.5$.

Much of the stellar mass density in galaxies $2.5 < z < 3.5$ could reside in red-selected galaxies, whose light is dominated by older, passively evolving stellar populations. For the $J_{110} - H_{160} > 1$ mag galaxies in the HUDF, we derive an upper limit on the stellar mass density of $\log(\rho^*/[M_\odot \text{Mpc}^{-3}]) = 7.4 \pm 0.3$, including the effect of our redshift-evolving mass limit, where our errors are derived from a Monte-Carlo simulation of the data. When we include our 50% incompleteness, our total stellar mass density becomes $\log(\rho^*/[M_\odot \text{Mpc}^{-3}]) = 7.7 \pm 0.3$. Poisson sampling of the 6 objects gives a factor of two error and therefore is the dominant source of uncertainty in the mass density estimate. We consider this measurement to be an upper limit on the mass density of distant evolved galaxies for two reasons: a) it is possible that some of our evolved galaxy candidates are in fact dusty starbursts, and b) because our two-component model fit incorporates an a priori upper limit on the mass-to-light ratio in the form of a maximally old SSP component (see §3).

Rudnick et al. (2003) derive a stellar mass density at $z = 2.80^{+0.40}_{-0.39}$ of $\log \rho_* = 7.5^{+0.1}_{-0.1}$ and at $z = 2.01^{+0.40}_{-0.41}$ of $\log \rho_* = 7.5^{+0.1}_{-0.1}$. Because our mass density provides an upper limit on the mass limit, we conclude that our derived mass density is consistent those of Rudnick et al. In this case, it may be that passively stellar populations dominate the stellar mass density. This is consis-

tent with the analysis of Dickinson et al. (2003) who used two-component star-formation history models to set an upper limit on the stellar mass density from passively evolving stellar populations hidden beneath the glare of younger stars in galaxies at $z < 3$. Dickinson et al. find that at $z \sim 2.5-3$ an upper limit on the stellar mass density of $\log(\rho^*/[M_\odot \text{Mpc}^{-3}]) = 7.89^{+0.20}_{-0.15}$. If this reflects reality, then based on our analysis, almost all of this mass density could reside in faint, red-selected galaxies at these redshifts. van Dokkum et al. (2006) found that at $z \sim 2$ red-selected galaxies with masses greater than $10^{11} M_\odot$ dominate the mass density. Our analysis of the HUDF galaxies suggests that at lower stellar masses red-selected galaxies still contribute significantly to the total mass budget.

Lastly, we stress that with only rest-frame UV and optical data, it is not possible to discriminate between those galaxies dominated by dusty starbursts and older stellar populations (e.g., Moustakas et al. 2004; Smail et al. 2002). Although the IRAC data does not resolve this degeneracy for all galaxies, we show that a sub-set of objects do have consistent best-fit results and we therefore use these objects in our analysis.

We wish to thank our colleagues at Steward Observatory for stimulating conversations. In particular we would like to thank George Rieke for useful comments, Xiaohui Fan for generously providing models of the IGM attenuation, and Karl Gordon for his suggestions and help with the dust models used in this work. AMS would also like to thank Richard Cool, Aleks Diamond-Stanic, Brandon Kelly, Juna Kollmeier, Andy Marble, John Moustakas, Jane Rigby and Yong Shi for helpful

discussions. Support for CJP was provided by NASA through the Spitzer Space Telescope Fellowship Program, through a contract issued by the Jet Propulsion Labora-

tory (JPL), California Institute of Technology under a contract with NASA. DJE is also supported by an Alfred P. Sloan Research Fellowship.

REFERENCES

- Adelberger, K. L., Steidel, C. C., Pettini, M., Shapley, A. E., Reddy, N. A., & Erb, D. K. 2005, *ApJ*, 619, 697
- Alexander, D. M., et al. 2003, *AJ*, 126, 539
- Baugh, C. M., Benson, A. J., Cole, S., Frenk, C. S., & Lacey, C. 2003, *The Mass of Galaxies at Low and High Redshift*, 91
- Beckwith, S. V. W., et al. 2006, *AJ*, 132, 1729
- Bell, E. F., McIntosh, D. H., Katz, N., & Weinberg, M. D. 2003, *ApJS*, 149, 289
- Bell, E. F., et al. 2004, *ApJ*, 608, 752
- Bertin, E., & Arnouts, S. 1996, *A&AS*, 117, 393
- Brammer, G. B., & van Dokkum, P. G. 2007, *ApJ*, 654, L107
- Bruzual, G., & Charlot, S. 2003, *MNRAS*, 344, 1000
- Calzetti, D., Armus, L., Bohlin, R. C., Kinney, A. L., Koornneef, J., & Storchi-Bergmann, T. 2000, *ApJ*, 533, 682
- Chary, R.-R., Teplitz, H. I., Dickinson, M. E., Koo, D. C., Le Floc'h, E., Marcillac, D., Papovich, C., & Stern, D. 2007, *ApJ*, 665, 257
- Chen, H.-W., & Marzke, R. O. 2004, *ApJ*, 615, 603
- Cimatti, A., et al. 2002, *A&A*, 381, L68
- Croton, D. J., et al. 2006, *MNRAS*, 365, 11
- Daddi, E., et al. 2005, *ApJ*, 626, 680
- Davé, R., et al. 2005, *astro-ph/0511532*
- De Lucia, G., Springel, V., White, S. D. M., Croton, D., & Kauffmann, G. 2006, *MNRAS*, 366, 499
- Dickinson, M., et al. 2000, *ApJ*, 531, 624
- Dickinson, M., Papovich, C., Ferguson, H. C., & Budavári, T. 2003, *ApJ*, 587, 25
- Dunlop, J. S., Cirasuolo, M., & McLure, R. J. 2007, *MNRAS*, 376, 1054
- Fan, X. 1999, *AJ*, 117, 2528
- Fazio, G. G., et al. 2004, *ApJS*, 154, 10
- Fontana, A., et al. 2006, *A&A*, 459, 745
- Förster Schreiber, N. M., et al. 2004, *ApJ*, 616, 40
- Franx, M., et al. 2003, *ApJ*, 587, L79
- Freedman, W. L., et al. 2001, *ApJ*, 553, 47
- Glazebrook, K., et al. 2004, *Nature*, 430, 181
- Hernquist, L., & Springel, V. 2003, *MNRAS*, 341, 1253
- Hopkins, A. M. 2004, *ApJ*, 615, 209
- Knudsen, K. K., et al. 2005, *ApJ*, 632, L9
- Kriek, M., et al. 2006, *astro-ph/0603063*
- Labbé, I., et al. 2003, *AJ*, 125, 1107
- Labbé, I., et al. 2005, *ApJ*, 624, L81
- Madau, P. 1995, *ApJ*, 441, 18
- McCarthy, P. J. 2004, *ARA&A*, 42, 477
- Mobasher, B., et al. 2005, *ApJ*, 635, 832
- Moustakas, L. A., et al. 2004, *ApJ*, 600, L131
- Papovich, C., Dickinson, M., & Ferguson, H. C. 2001, *ApJ*, 559, 620
- Papovich, C., et al. 2004, *ApJS*, 154, 70
- Papovich, C., et al. 2006, *ApJ*, 640, 92
- Quadri, R., et al. 2007, *ApJ*, 654, 138
- Rubin, K. H. R., van Dokkum, P. G., Coppi, P., Johnson, O., Förster Schreiber, N. M., Franx, M., & van der Werf, P. 2004, *ApJ*, 613, L5
- Reddy, N. A., Erb, D. K., Steidel, C. C., Shapley, A. E., Adelberger, K. L., & Pettini, M. 2005, *ApJ*, 633, 748
- Rudnick, G., et al. 2003, *ApJ*, 599, 847
- Rudnick, G., et al. 2006, *ApJ*, 650, 624
- Saracco, P., Giallongo, E., Cristiani, S., D’Odorico, S., Fontana, A., Iovino, A., Poli, F., & Vanzella, E. 2001, *A&A*, 375, 1
- Shapley, A. E., Steidel, C. C., Adelberger, K. L., Dickinson, M., Giavalisco, M., & Pettini, M. 2001, *ApJ*, 562, 95
- Shapley, A. E., Steidel, C. C., Erb, D. K., Reddy, N. A., Adelberger, K. L., Pettini, M., Barmby, P., & Huang, J. 2005, *ApJ*, 626, 698
- Smail, I., Owen, F. N., Morrison, G. E., Keel, W. C., Ivison, R. J., & Ledlow, M. J. 2002, *ApJ*, 581, 844
- Somerville, R. S., Primack, J. R., & Faber, S. M. 2001, *MNRAS*, 320, 504
- Somerville, R. S., et al. 2004, *ApJ*, 600, L135
- Spergel, D. N., et al. 2003, *ApJS*, 148, 175
- Thompson, R. I., et al. 2005, *AJ*, 130, 1
- Toft, S., van Dokkum, P., Franx, M., Thompson, R. I., Illingworth, G. D., Bouwens, R. J., & Kriek, M. 2005, *ApJ*, 624, L9
- van Dokkum, P. G., et al. 2003, *ApJ*, 587, L83
- van Dokkum, P. G., et al. 2006, *ApJ*, 638, L59
- Webb, T. M. A., et al. 2006, *ApJ*, 636, L17
- Weinberg, D. H., Davé, R., Katz, N., & Hernquist, L. 2004, *ApJ*, 601, 1
- Williams, R. E., et al. 1996, *AJ*, 112, 1335
- Wilson, G., et al. 2004, *ApJS*, 154, 107
- Wilson, G., et al. 2007, *ApJ*, 660, L59
- Witt, A. N., & Gordon, K. D. 2000, *ApJ*, 528, 799
- Yan, H., & Windhorst, R. A. 2004, *ApJ*, 612, L93
- Yan, H., et al. 2004a, *ApJ*, 616, 63
- Yan, L., et al. 2004b, *ApJS*, 154, 75